Progress In Electromagnetics Research, PIER 37, 31–78, 2002

MICROWAVE ANALYTICAL BACKSCATTERING MODELS FROM RANDOMLY ROUGH ANISOTROPIC SEA SURFACE—COMPARISON WITH EXPERIMENTAL DATA IN C AND KU BANDS

C. Bourlier

Ecole Polytechnique de l'Université de Nantes
Bat. IRESTE
IRCCyN: UMR n° 6597 CNRS, Division SETRA
Rue Christian Pauc, La Chantrerie, BP 50609
44306 NANTES Cedex 3, France

G. Berginc

DS/DFO, THALES Optronique
Rue Guynemer
BP 55, 78283 Guyancourt Cedex, France

Abstract—The small slope approximation (SSA) and the Kirchhoff approach (KA) are applied to the prediction of microwave sea surface backscatter for both Ku and C bands for various wind speeds and incident angles. Numerical results are obtained assuming a non-directional surface wavenumber spectrum and compared with azimuthally averaged C- and Ku-band radar backscattering data. The KA can be obtained rigorously for a perfectly-conducting surface, whereas for a dielectric surface, either the KA of order one (KA1) or the stationary phase (SP) method can be used. Numerical results are obtained assuming a non-directional surface wavenumber spectrum and compared with azimuthally C and Ku bands radar backscattering data for incidence angles of interest for remote sensing. Since the SSA and KA formulations are expressed in polar coordinates, the backscattering coefficient is expressed in terms of surface height autocorrelation and its derivatives of one- and second- orders computed from integrating the sea spectrum multiplied by Bessel functions of the first kind. This allows to have for KA and first-order SSA (SSA-1), a single numerical integration over the radial distance instead of four, when the cartesian coordinates is chosen. Moreover, the azimuthal harmonic magnitudes of the backscattering coefficient according to the wind direction can

be performed separately. For an isotropic sea surface assumed to be perfectly conducting where the KA is valid, the deviation between SSA and KA models is smaller than the one computed from the SP model for HH polarization. For the VV polarization, the difference is greater, since the polarization term of SSA is given by the small perturbation method, whereas for the KA approach, it is equal to the Fresnel coefficient. For an anisotropic sea surface, the comparison of KA with SSA-1 leads to the same conclusion. The isotropic part and the second azimuthal harmonic of the backscattering coefficient are also compared with empirical backscattering models CMOD2-I3 and SASS-II valid in C and Ku bands, respectively.

1. INTRODUCTION

Observations of microwave backscattering from the sea are important for understanding the air-sea fluxes that arise from wind acting on the roughened surface of the ocean and for remote sensing. Analytical models can be used to compute the normal radar cross section (NRCS) from stationary sea surface. We can quote the Kirchhoff approach (KA) [1–4], the small-perturbation model (SPM) [2, 5], the phase perturbation model [6, 7] (PPM), the full wave method (FWM) [8], and recently the small slope approximation [9–16] (SSA) developed by Voronovich.

The most widely used method for relating microwave scattering to surface roughness is composite-roughness [17] theory. This model introduces a scale-dividing parameter k_d separating small- and large-scale components of the roughness which can be arbitrarily chosen within wide limits. There are therefore two terms in the NRCS. The first one corresponds to the geometrical optics solution (KA in high-frequency limit valid for a very rough surface) for the large-scale component (specular reflections), and the second one corresponds to the Bragg scattering solution (SPM solution valid for a slightly rough surface) for the small-scale component modulated by tilts of large-scale waves. The advantage of this method is that it is easily applied. As illustrated [11], one disadvantage is that the predictions are dependent on how the surface is partitioned within the choice of k_d. A second one is the difficulty in establishing the accuracy of the theory.

The small slope approximation (SSA) has not the above-mentioned drawbacks. For the Gaussian statistics of roughness, the result can be expressed strictly in terms of a roughness spectrum. The SSA can be applied to an arbitrary wavelength, provided the tangent of grazing angles of incident/scattered radiation sufficiently exceeds rms (root mean square) slopes of roughness. The SSA represents a regular expansion of the scattering amplitude (or the scattering cross section) in terms of the roughness slope, and both the first- and the second-order results of SSA calculations can be obtained. When the difference between the first- and the second-order results is relatively small, one can be sure that the solution of the scattering problem is accurate for the first-order.

Recently the Kirchhoff approach (KA) have been re-examined by Bourlier et al [18] for an anisotropic perfectly conducting surface in backscattering configuration. It is important to note that the KA is often confused with the stationary phase (SP) method which is a particular case of KA. Indeed, the SP formulation assumes that the resulting scattering field expression contains only contributions from

specular points in the surface. This allows to remove the statistical dependence of the surface slopes involving that the integrations over the surface slopes is not required. The NRCS depends then only on the surface height joint characteristic function equal to the Fourier transform of the surface height joint pdf (probability density function). Unlike, with the KA approach, the NRCS is formulated in terms of a surface height characteristic function, and in terms of expected values for the integrations over the surface slopes. As depicted [18] (see Figures 3–4), for scattering angles larger than twenty degrees where the Bragg scattering regime is involved, the NRCS computed from KA is more greater than the one performed with SP. This behavior is similar to the one observed by Voronovich [11].

For a dielectric surface, the KA approach can not be tractable analytically since the dependence over the surface slopes is a complicated function [18]. To have therefore a formulation of KA for a dielectric rough surface, Bourlier et al [19] extended the scalar approximation (SA) developed by Ulaby et al [2] to an anisotropic surface. The SA is obtained by expanding the Kirchhoff integral over the surface slopes and keeping only the terms of first order. With these models, the calculation of the backscattering coefficient used a surface height and slope joint pdf assumed to be Gaussian given by [20, page 272]. It is expressed from a covariance matrix of six-dimension, where the elements depend on the surface height autocorrelation function in polar coordinates and its first and second derivatives. The autocorrelation function [21] is defined from the general behavior of ocean-like spectrum proposed by Elfouhaily [22].

Considering an anisotropic sea surface, this paper compares the normal radar cross section (NRCS) computed from the Kirchhoff (KA) and scalar (SA) models with the small slope approximation (SSA). Numerical models are also compared with measurements from the CMOD2-I3 [23, 24] and Ku SASS-II [25] backscattering models valid for C and Ku bands, respectively.

The paper is organized as follows. Section 2 presents the backscattering coefficient derived from KA, SA, and SSA models by considering the sea spectrum symmetry [22]. In Section 3, the Elfouhaily et al [22] spectrum is studied. To analyze the sea surface roughness (product $k\omega$ with k the incident wave number and ω the surface rms heights), the surface rms heights and slopes are computed versus the wind speed. The slope surface is directly related to the capillary waves which involves the Bragg scattering solution. This region is also affected by the spreading function of the spectrum. The Cox and Munk models [27] in upwind and crosswind directions are compared with the variance slopes computed from integrating the sea

spectrum multiplied by the square wave number. The shadowing effect is also analyzed [20]. In Section 4, numerical results are presented for a perfectly-conducting and dielectric sea surfaces and are compared with CMOD2-I3 [23, 24] and SASS-II [25] backscattering models valid in C and Ku bands, respectively. From measurements made in microwave band [23–26] for co-polarizations pq (VV and HH), the NRCS is model as $\sigma_{pq} = \sigma^0_{pq} + \sigma^1_{pq}\cos\phi + \sigma^2_{pq}\cos(2\phi)$ which depends on the scattering angle, the wind speed, and the wind direction ϕ.

2. BACKSCATTERING MODELS

This section presents the Kirchhoff (KA), scalar (SA) and small slope (SSA) approximations for the derivation of the normal radar cross section (NRCS). The KA is valid if the radius of curvature at every point on the surface is large relative to the electromagnetic wavelength λ, and if the correlation length L_c is larger than λ [1–3]. The KA is used as a starting point for high-frequency analysis when the geometric optics approximation is obtained by applying the stationary phase method. The SA have similar assumptions as KA and assumes that the surface rms slopes are smaller than 0.25 [2] which is verified for the sea surface. The SSA can be applied for an arbitrary wavelength, provided the tangent of grazing angles of incident/scattered radiation sufficiently exceeds the rms slopes [9–11].

For a backscattering configuration, Bourlier et al [18,19] showed that the statistical shadowing function [20] can be ignored in the KA and SA computations. Thus, the shadowing effect is omitted and Section 3 will prove for the sea surface that this assumption can be easily verified.

2.1. Incoherent Backscattering Coefficient from Kirchhoff Approximation

With the Kirchhoff approach, the scattered field is written in terms of the tangential field on rough surface. The surface field is then approximated by the field that would be present if the rough surface was replaced by a planar surface tangential to the point of interest. With this assumption, the backscattered field is expressed as [2]

$$\vec{E}^s = K_1\vec{n}_s \wedge \iint \left[\vec{n}\wedge\vec{E} - \eta\vec{n}_s\wedge(\vec{n}\wedge\vec{H})\right]\exp(j2K\vec{n}_s\cdot\vec{r})dS \qquad (1)$$

$K_1 = jK\exp(-jKR_0)/(4\pi R_0)$, with K the wave number in the medium where the field is evaluated, R_0 range from the center of the

illuminated area S to the point of observation, $\vec{n}_s$ the unit vector in the scattered direction defined in spherical coordinates as

$$\vec{n}_s = \sin\theta\cos\varphi\vec{x} + \sin\theta\sin\varphi\vec{y} + \cos\theta\vec{z} \tag{1a}$$

where $(\vec{x}, \vec{y}, \vec{z})$ are unit vectors in cartesian coordinates. $\vec{r} = x\vec{x} + y\vec{y} + z\vec{z}$ is the vector indicating the location of the surface point according to the center of the illuminated area.

The incoherent scattering coefficient σ_{pq} (p and q denote the state polarization which is either vertical V or horizontal H) for an extended target can be written as [2]

$$\sigma_{pq} = \frac{4\pi R_0^2[\langle E_{pq}^S E_{pq}^{S\prime *}\rangle - |\langle E_{pq}^S\rangle|^2]}{S|E_0|^2} \tag{2}$$

Substituting (1) into (2), Bourlier et al [18] showed in polar coordinates for a perfectly conducting surface

$$\sigma^{KA} = \frac{(K\cos\theta)^2}{\pi}\int_0^\infty r dr \int_0^{2\pi} d\Phi \langle\ldots\rangle^{KA} \exp[2jrK\sin(\theta)\cos(\phi-\Phi)] \tag{3}$$

where the symbol $\langle\ldots\rangle^{KA}$ denote the ensemble average under the Kirchhoff approximation (exponent KA) given by

$$\begin{aligned}\langle\ldots\rangle^{KA} &= \exp[-K_\omega^2(1-f_0)][1 + j\chi_1(\sigma_X\tan\theta) + \chi_2(\sigma_X\tan\theta)^2] \\ &\quad - \exp(-K_\omega^2)\end{aligned} \tag{4}$$

with

$$K_\omega = 2K\omega\cos\theta \tag{4a}$$

$$\chi_1 = 2K_\omega \times \left(cf_1 + \frac{s\sigma_Y f_{16}}{\sigma_X}\right) \tag{4b}$$

$$\chi_2 = c^2 f_2 + \frac{s^2\sigma_Y^2 f_{56}}{\sigma_X^2} + \frac{2sc\sigma_Y f_{36}}{\sigma_X} - K_\omega^2\left(cf_1 + \frac{s\sigma_Y f_{16}}{\sigma_X}\right)^2 \tag{4c}$$

$$c = \cos(\phi-\Phi) \qquad s = \sin(\phi-\Phi) \tag{4d}$$

In (4), the exp[...] first term corresponds to the surface height joint characteristic function obtained from a surface height joint pdf assumed to be Gaussian. The second term $\exp(-K_\omega^2)$ gives the contribution of the coherent component.

The normalized functions $\{f_0, f_1, f_2, f_{16}, f_{36}, f_{56}\}$ are given by

$$\begin{cases} f_0 = R_0/\omega^2 \\ f_2 = -R_2/\sigma_X^2 \\ f_{56} = -C_{56}/\sigma_Y^2 \end{cases} \quad \begin{cases} f_1 = -R_1/(\omega\sigma_X) \\ f_{16} = -C_{16}/(\omega\sigma_Y) \\ f_{36} = -C_{36}/(\sigma_Y\sigma_X) \end{cases} \tag{5}$$

where $\{R_0, R_1, R_2, R_{16}, R_{36}, R_{56}\}$ are expressed as [20, page 272]

$$\begin{cases} R_0 = R_{00} - \cos(2\Phi)R_{02} \\ R_1 = R_{10} - \cos(2\Phi)R_{12} \\ R_2 = R_{20} - \cos(2\Phi)R_{22} \end{cases} \qquad R_{ij} = \frac{d^i R_{0j}}{dr^i} \tag{5a}$$

$$\begin{cases} C_{16} = \dfrac{2R_{02}\sin(2\Phi)}{r} \\ C_{36} = \dfrac{2\sin(2\Phi)}{r^2}(rR_{12} - R_{02}) \\ C_{56} = \dfrac{R_{10}}{r} + \dfrac{\cos(2\Phi)}{r^2}(4R_{02} - rR_{12}) \end{cases} \tag{5b}$$

$$\begin{cases} \sigma_X^2 = \alpha + \beta\cos(2\phi) \\ \sigma_Y^2 = \alpha - \beta\cos(2\phi) \\ \sigma_{XY}^2 = -\beta\sin 2\phi \end{cases} \quad \begin{cases} \alpha = \dfrac{\sigma_x^2 + \sigma_y^2}{2} \\ \beta = \dfrac{\sigma_x^2 - \sigma_y^2}{2} \end{cases} \tag{5c}$$

In (5a), $R_0(r, \Phi)$ is the surface height two-dimensional autocorrelation function in polar coordinates, whereas $-R_2$ is the surface slope two-dimensional autocorrelation function. $\{R_{00}(r), R_{02}(r)\}$ represent the isotropic and anisotropic parts of R_0, and Φ the azimuthal direction which characterizes the anisotropic effect. In (5c), $\{\sigma_X^2 = -R_2(0, \phi), \sigma_Y^2 = -C_{56}(0, \phi)\}$ denote the surface slope variances in the $\{(0X), (0Y)\}$ directions, respectively, and $\sigma_{XY}^2 = -C_{36}(0, \phi)$ the surface slope cross-variance. $\{\sigma_x^2, \sigma_y^2\}$ are the slope variances in upwind and crosswind directions. As depicted Figure 1, ϕ is the wind direction. $\omega^2 = R_0(0, \Phi) = R_{00}(0)$ is the surface height variance with $R_{02}(0) = 0$.

Since the surface is assumed to be perfectly conducting, the NRCS in VV and HH polarizations are equal. In (5a), the functions $R_{ij}(r)$ will be expressed from the sea spectrum in Section 3.3.

2.2. Incoherent Backscattering Coefficient from Scalar Approximation

The scalar approximation consists of approximating the Kirchhoff integral by a series expansion about the origin of the slopes and retains

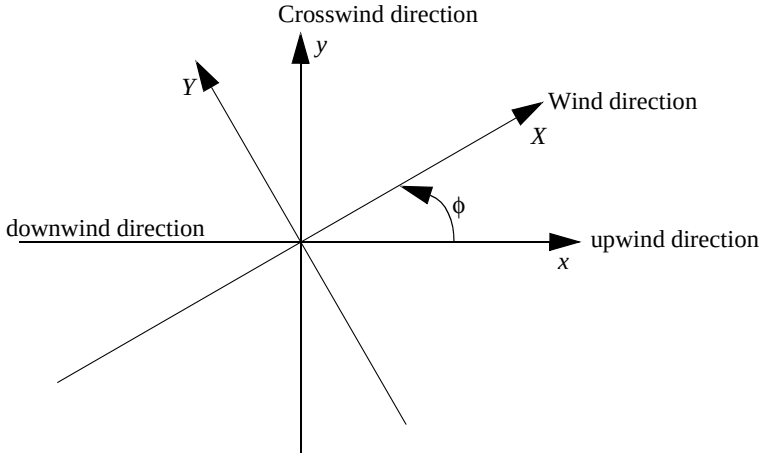

Figure 1. Indication of the different wind directions.

only the first-order term. From Ulaby et al [2, chapter 12] Bourlier et al [19] proved for a Gaussian anisotropic dielectric random surface that the backscattering coefficient has the similar form as (3) where the ensemble average $\langle \ldots \rangle^{SA}$ is

$$\begin{aligned}\langle \ldots \rangle^{SA} \;=\; & \exp[-K_\omega^2(1-f_0)][|R_{H,V}|^2 + j\chi_1(\sigma_X \tan\theta) \\ & \cdot\Re(R_{H,V}R_{H1,V1})] - \exp(-K_\omega^2)|R_{H,V}|^2 \end{aligned} \tag{6}$$

where $\Re$ denotes the real part. K_ω, χ_1, $\{c, s\}$ and $\{f_0\}$ are given by (4a), (4b), (4d) and (5), respectively. $R_{H,V}$ are the Fresnel coefficients in V (for VV polarization) and H (for HH polarization) polarizations defined as

$$R_V = \frac{\varepsilon_r \cos\theta - (\varepsilon_r - \sin^2\theta)^{1/2}}{\varepsilon_r \cos\theta + (\varepsilon_r - \sin^2\theta)^{1/2}} \quad R_H = \frac{\cos\theta - (\varepsilon_r - \sin^2\theta)^{1/2}}{\cos\theta + (\varepsilon_r - \sin^2\theta)^{1/2}} \tag{6a}$$

with ε_r the permittivity of the surface. The permittivity of the air is assumed to be equal to one.

In (6), $R_{H1,V1}$ are expressed as

$$R_{V1} = \frac{\cos\theta[1 - \varepsilon_r + R_V(1+\varepsilon_r)]}{\varepsilon_r \cos\theta + (\varepsilon_r \sin^2\theta)^{1/2}} \quad R_{H_1} = \frac{2\cos\theta R_H}{\cos\theta + (\varepsilon_r - \sin^2\theta)^{1/2}} \tag{6b}$$

In (6), to have a form as $+j\chi_1(\sigma_X \tan\theta)$, the $\{R_{V1}, R_{H1}\}$ coefficients have been multiplied by $-1/(\tan\theta)$. Comparing (6) with (4) without the second-order term $(\sigma_X \tan\theta)^2$, a similar behavior of the ensemble

average is found. For a perfectly conducting surface, we have $R_V = 1,\ R_H = -1,\ R_{V1} = 0, R_{H1} = 0$, and for $\sigma_X \tan\theta \ll 1$ (slope standard deviation σ_X much smaller than the slope $\cot\theta$ of the scattered field), the ensemble averages $\{\langle\ldots\rangle^{SA}, \langle\ldots\rangle^{KA}\}$ are equal.

With the stationary (SP) method [2], the ensemble average (exponent SP) is

$$\langle\ldots\rangle^{SP} = \{\exp[-K_\omega^2(1-f_0)] - \exp(-K_\omega^2)\}|R_{H,V}|^2/(\cos\theta)^4 \qquad (7)$$

It is important to note in [4] that the ensemble average given by (7) is multiplied by $(\cos\theta)^4$ inferring on the level of the incoherent scattering coefficient.

From (7) and (4), for a perfectly conducting surface ($|R_{H,V}| = 1$), we can see that $\langle\ldots\rangle^{SP} \neq \langle\ldots\rangle^{KA}$. Therefore, the NRCS computed from KA and SP methods are different excepted for $\chi_1 = \chi_2 = 0$ with $(\cos\theta)^4 = 1$. On the other hand, from (4b)–(4c) this is similar to consider $\{f_1, f_2, f_{16}, f_{36}, f_{56}\} = 0$ involving that the correlation between the surface heights-slopes ($\{f_1, f_{16}\} = 0$) and slopes-slopes ($\{f_2, f_{36}, f_{56}\} = 0$) is assumed to be equal to zero.

2.3. Incoherent Backscattering Coefficient from Small Slope Approximation

The small-slope approximation is appropriate for scattering from both large- (the SP regime), intermediate- and small-scale (the Bragg regime) roughness within a single theoretical scheme. Both the lowest-order approximation (which we refer to as the SSA-1) and the next-order approximation (the SSA-2), which includes corrections to the SSA-1, can be calculated. The SSA was verified in a number of numerical simulations [15–16].

In [11], Voronovich proposed a formulation of the backscattering coefficient which combines both SSA-1 and SSA-2. The ensemble average from SSA approach $\langle\ldots\rangle^{SSA}$ can be then written as

$$\langle\ldots\rangle^{SSA} = |B_{H,V}|^2\{\exp[-K_\omega^2(1-f_{0M})] - \exp(-K_\omega^2)\} \qquad (8)$$

with

$$B_V = \frac{(\varepsilon_r - 1)[\sin^2\theta(1-\varepsilon_r) - \varepsilon_r]}{[\varepsilon_r\cos\theta + (\varepsilon_r - \sin^2\theta)^{1/2}]^2} \quad B_H = R_H \qquad (8a)$$

This formulation is weakly different that the one proposed in [9, 10, 12–14], and presents the drawback that the cross-polarization is not taken into account with accuracy. On the other hand, the computer time is less important for the second order.

In (8), $f_{0M}(r,\Phi)$ is the normalized modified surface height autocorrelation function in polar coordinates which contains the effect of SSA-2. For a backscattering configuration, in cartesian coordinates $\vec{r}^T=[x\ y]$, $f_{0M}(\vec{r})$ is defined from the Fourier transform of the surface roughness spectrum $\Psi(\vec{\xi})$ as (equation (10) of [11] with $\vec{k}_s=-\vec{k}_0$ for the backscattering case)

$$f_{0M}(\vec{r})=\frac{1}{\omega^2}\iint\left|1-\frac{M_{V,H}(\vec{\xi})}{8B_{V,H}\cos\theta}\right|^2\Psi(\vec{\xi})\exp(j\vec{\xi}\cdot\vec{r})d\vec{\xi} \tag{9}$$

with

$$M_{V,H}(\vec{\xi})=B_{1V,1H}(-\vec{k}_0-\vec{\xi})+B_{1V,1H}(\vec{k}_0+\vec{\xi})+4KB_{V,H}\cos\theta \tag{9a}$$

where $\vec{k}_0=K(\vec{x}\cos\phi\sin\theta+\vec{y}\sin\phi\sin\theta)$ is the horizontal wave vector of the incident field according to the wind direction.

The polarization terms $B_{1V,1H}$ in VV and HH polarizations are defined as (see appendix of [11])

$$\begin{aligned}B_{1V}(\vec{\xi}) &= \frac{2(\varepsilon_r-1)}{(\varepsilon_r q_{01}+q_{02})^2}\left\{\frac{1-\varepsilon_r}{\varepsilon_r q_{\xi1}+q_{\xi2}}\left[\varepsilon_r k_0^2\xi^2-q_{02}^2\frac{(\vec{k}_0\cdot\vec{\xi})^2}{k_0^2}\right]\right.\\ &\left.+\varepsilon_r k^2 q_{02}+q_{02}^2(q_{\xi1}-q_{\xi2})\right\} \qquad (9b)\\ B_{1H}(\vec{\xi}) &= \frac{2(\varepsilon_r-1)k^2}{(q_{01}+q_{02})^2}\left\{\frac{1-\varepsilon_r}{\varepsilon_r q_{\xi1}+q_{\xi2}}\left[\xi^2-\frac{(\vec{k}_0\cdot\vec{\xi})^2}{k_0^2}\right]-q_{02}-q_{\xi1}+q_{\xi2}\right\} \qquad (9c)\end{aligned}$$

where

$$\left\{\begin{array}{ll} q_{01}=K\cos\theta & q_{02}=K(\varepsilon_r-\sin^2\theta)^{1/2}\\ q_{\xi1}=K(1-\xi^2/K^2)^{1/2} & q_{\xi2}=K(\varepsilon_r-\xi^2/K^2)^{1/2}\\ \xi^2=\vec{\xi}\cdot\vec{\xi} & k_0^2=\vec{k}_0\cdot\vec{k}_0=(K\sin\theta)^2\end{array}\right. \tag{9d}$$

From (9b)–(9c), we get $B_{1V,1H}(-\vec{\xi})=B_{1V,1H}(\vec{\xi})$, which leads from (9a) to

$$1-\frac{M_{V,H}(\vec{\xi})}{8B_{V,H}\cos\theta}=\frac{1}{2}\left(1-\frac{B_{1V,1H}(\vec{k}_0+\vec{\xi})}{2K\cos\theta}\right) \tag{10}$$

We can note that $B_{1V,1H}(\vec{k}_0+\vec{\xi})/K$ is dimensionless.

Substituting (10) into (9), the normalized modified surface height autocorrelation function becomes in polar coordinates

$$f_{0M}(r,\Phi) = \frac{1}{4\omega^2}\int_0^{2\pi} d\psi \int_0^{\infty} \left|1 - \frac{B_{1V,1H}(\xi,\psi)}{2K\cos\theta}\right|^2 \cdot S(\xi,\psi)\exp[j\xi r\cos(\psi-\Phi)]d\xi \tag{11}$$

where $S(\xi,\psi) = \xi \times \Psi(\xi,\psi)$ is the sea spectrum in polar coordinates.

The fact to substitute in (9b)–(9c) $\vec{\xi}$ by $\vec{k}_0 + \vec{\xi}$ involves that

$$\begin{cases} \vec{k}_0 \cdot \vec{\xi} \rightarrow k_0^2 + \vec{k}_0 \cdot \vec{\xi} = k_0^2 + k_0\xi\cos(\psi-\phi) \\ \xi^2 \rightarrow (\vec{k}_0 + \vec{\xi})^2 = k_0^2 + \xi^2 + 2k_0\xi\cos(\psi-\phi) \end{cases} \tag{11a}$$

In (10), for $\vec{\xi} = \vec{0}$, we can verified that $-B_{1V,1H}(\vec{k}_0+\vec{\xi})/\,(2K\cos\theta) = 1$, meaning that the square modulus term in (11) is equal to four. With $S(\xi,\psi) = M(\xi)[1+\Delta(\xi)\cos(2\psi)]/(2\pi)$ (general behaviour of the sea spectrum, see Section 3.1), the integration over ψ can be then performed analytically [21], yielding $f_{0M}(r,\Phi) = f_0(r,\Phi)$. This assumption is similar to consider only the first term of the small slope approximation. Comparing therefore (8) $\langle\ldots\rangle^{SSA}$ with (6) $\langle\ldots\rangle^{SA}$ ensemble averages, the backscattering coefficients are different within the polarizations terms (6a) $R_{V,H}$ and (8a) $B_{V,H}$, respectively. For $\theta = 0$, we have $|R_V(0)| = |R_H(0)| = |B_V(0)| = |B_H(0)|$ meaning that the backscattering coefficients are equal.

Since the sea spectrum $S(\vec{\xi})$ is even and $B_{1V,1H}(\vec{\xi})$ is not generally an even function with (11a) variable transformations, the global spectrum is not even with respect to $\vec{\xi}$ which involves that $f_{0M}(r,\Phi)$ is not symmetrical as $f_0(r,\Phi)$.

In Figure 2, the Fresnel coefficients $\{|R_{V,H}|^2\}$ and $\{\Re(R_{H,V}R_{H1,V1})\}$ in VV and HH polarizations are plotted versus the scattering angle. The sea permittivities [28] are equal to $\varepsilon_r = 67 + j35$ ($f = 5.3\,\text{GHz}$ in C band) and $\varepsilon_r = 47 + j38$ ($f = 14\,\text{GHz}$ in Ku band). We observe that $\{|R_V|^2, |R_H|^2\}$, are larger than $\{\Re(R_{H,V}R_{H1,V1})\}$. For the SSA approach, $B_H = R_H$ and $|B_V|^2$ is not represented because is greater than one (there is no restriction on the modulus of B_V since this is not a reflection coefficient).

3. SEA SPECTRUM

The computation of the backscattering coefficient requires the knowledge of either the sea spectrum or the sea surface height autocorrelation function obtained from the Fourier transform of the

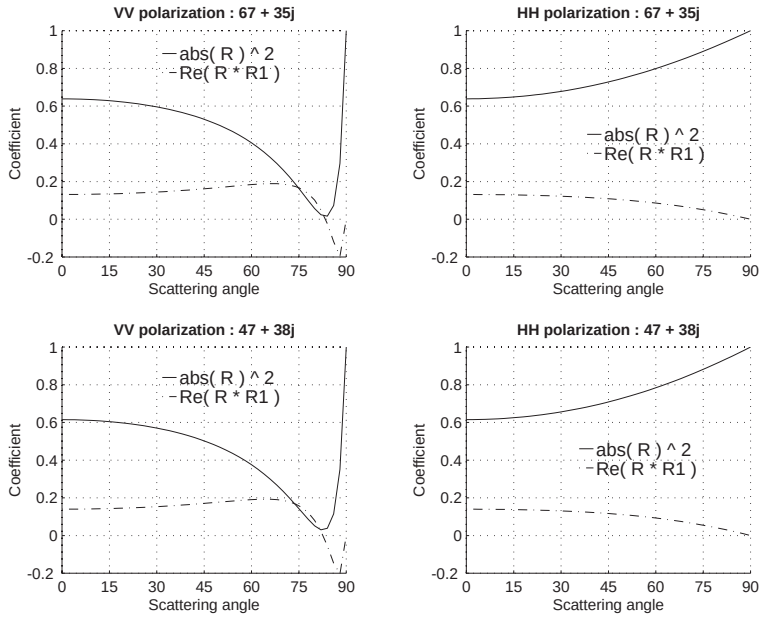

Figure 2. Fresnel coefficients $\{|R_{V,H}|^2\}$ and $\{\Re(R_{H,V}R_{H1,V1})\}$ in VV and HH polarizations versus the scattering angle. The sea permittivity is $\varepsilon_r = 67 + j35$ and $\varepsilon_r = 47 + j38$.

sea spectrum. The ensemble average with KA (equation (4)) and SA (equation (6)) can be studied within the roughness parameters $K_\omega = 2K\omega\cos\theta$ and $\sigma_X \tan\theta$. K is the incident wave number, ω the surface height standard deviation, σ_X the rms of the surface slopes in the wind direction, and θ the scattering angle. Indeed, according to the value of these roughness parameters, the integrations over $\{r, \Phi\}$ of (3) scattering coefficient can be simplified.

In this section, these parameters are analyzed from the Elfouhaily et al spectrum [22] in microwave region. The shadowing effect is also addressed.

3.1. Elfouhaily et al Sea Spectrum

The Pierson spectrum [29] is one of the first spectra published in the literature to describe capillary and gravity waves. The gravity region has been modified by adding the JONSWAP behavior [30] where the fetch effect is provided. Since the capillary region does not fit some physical criteria as the surface slope variance, its behavior has been investigated. We can quote the Apel spectrum [31] which is a synthesis

of works done in 80's and 90's. Unfortunately as shown Elfouhaily et al [22], this spectrum does not agree with the slope model proposed by Cox and Munk [27]. This discrepancy is due to an inaccuracy of the capillary waves. The set of these aspects are summarized in [21].

In our simulations we used the Elfouhaily et al model for the sea roughness spectrum, which was recently developed based on available field and wave-tank measurements, along with physical arguments. It is important to note that this model was developed without any relation to remote-sensing data. We avoided some deficiencies of this spectral model found in [32].

Elfouhaily et al assume a directional spectrum $S(k,\psi)$ defined in polar coordinates as

$$S(k,\psi) = M(k)f(k,\psi) \tag{12}$$

where

$$M(k) = (B_L + B_H)/k^3 \tag{12a}$$

and

$$f(k,\psi) = [1 + \Delta(k)\cos(2\psi)]/(2\pi) \tag{12b}$$

In (12), $M(k)$ denotes the non-directional spectrum (isotropic part) modulated by the $f(k,\psi)$ spreading function. In (12a), B_L and B_H are the respective contributions from low (gravity waves) and high (capillary waves) wavenumbers.

The low-wavenumber curvature spectrum B_L is assumed to obey

$$B_L(k) = \alpha_p c(k_p) F_p/[2c(k)] \tag{13}$$

The parameters in (13) are dependent on u_{10}, the wind speed measured at an altitude of ten meters above the sea, and on inverse wave age $\Omega \approx u_{10}/c(k_p)$ where $c(k)$ is the phase speed and k_p is the wave number of the spectral peak. In (13)

$$\begin{cases} \alpha_p = 6 \times 10^{-3}\Omega^{1/2} \quad k_p = g\Omega^2/u_{10}^2 \\ c(k) = [g(1 + k^2/k_m^2)]^{1/2} \end{cases} \tag{14}$$

where g is the gravitational constant and $k_m = 363\,\mathrm{rad/m}$. The function F_p in (13) is given by

$$F_p = \gamma^{\Gamma} \times \exp[-(5k^2)/(4k_p^2)] \times \exp\{-\Omega[(k/k_p)^{1/2} - 1]/\sqrt{10}\} \tag{15}$$

where

$$\kappa = \begin{cases} 1,7 & 0,84 < \Omega \le 1 \\ 1,7 + 6\log\Omega & 1 < \Omega \le 5 \end{cases} \tag{15a}$$

$$\Gamma = \exp\{-[(k/k_p)^{1/2} - 1]^2/(2\delta^2)\} \quad \delta = 0,08(1 + 4/\Omega^3)$$

The assumed contribution to (12a) at high wavenumbers is

$$B_H(k) = \alpha_m c(k_m) F_m / [2c(k)] \tag{16}$$

where

$$\alpha_m = 10^{-2} \begin{cases} 1 + \ln[u_f/c(k_m)] & u_f \leq c(k_m) \\ 1 + 3\ln[u_f/c(k_m)] & u_f > c(k_m) \end{cases} \tag{17}$$
$$F_m = \exp\{-[(k/k_m) - 1]^2/4\}$$

with $c(k_m) = 23\,\mathrm{cm/s}$. The data used to formulate (17) are limited to wind speeds $u_{10} < 17.2\,\mathrm{m/s}$. For a neutrally stable atmosphere, the friction speed u_f is obtained in [22] by using the relationships

$$C_{10} = (0,8 + 0,064u_{10}) \times 10^{-3} \quad u_f = C_{10}^{1/2} u_{10} \tag{18}$$

where the units of u_{10} and u_f are m/s.

In this study, to obtain spectra consistent with those presented in [22], an additional factor $\exp[-(5k^2)/(4k_p^2)]$ is inserted on the right-hand side of (16).

In (12b), the function $\Delta(k)$ which characterizes the spreading function is assumed to be equal to

$$\Delta(k) = \tanh\{a_0 + a_p[c(k)/c(k_p)]^{2,5} + a_m[c(k_m)/c(k)]^{2,5}\} \tag{19}$$

where

$$a_0 = 0,173 \quad a_p = 4 \quad a_m = 0,13u_f/c(k_m) \tag{19a}$$

For the simulations, a fully developed sea is assumed which is similar to take an inverse wave age Ω equal to 0.84.

In Figures 3–5, the isotropic parts $\{k^{-3}(B_L + B_H), k^{-3}B_L\}$, the curvature isotropic parts $\{B_L + B_H, B_L\}$, and the angular part $\Delta(k)$ of the sea spectrum are plotted versus the wave number k, respectively, with wind speeds $u_{10} = \{5, 15\}\,\mathrm{m/s}$. The vertical lines in Figures 4–5 are placed at wave numbers equal to $k = 2K\sin\theta$ with $\theta = \{30, 60\}^\circ$ for frequencies $f = 5.3\,\mathrm{GHz}$ (dashed lines) and $f = 14\,\mathrm{GHz}$ (dashdot lines). As depicted Figure 3, when the wind speed increases, the maximum (equal from [21] to $0.00193/k_p^2$ with $k_p = g\Omega^2/u_{10}^2$) of the spectrum increases with a shift toward low-wavenumbers (equal from [21] to $0.98k_p^2$) because the contribution of the gravity waves increases. Unlike Figure 4 where the curvature spectrum is represented, we observe that the total spectrum is weakly affected by the capillary region (B_H term) since $k^{-3}(B_L + B_H) \approx k^{-3}B_L$. Indeed from Figure 4, for the curvature spectrum, the capillary region takes place and strongly increases with the wind speed. In microwave frequencies, this

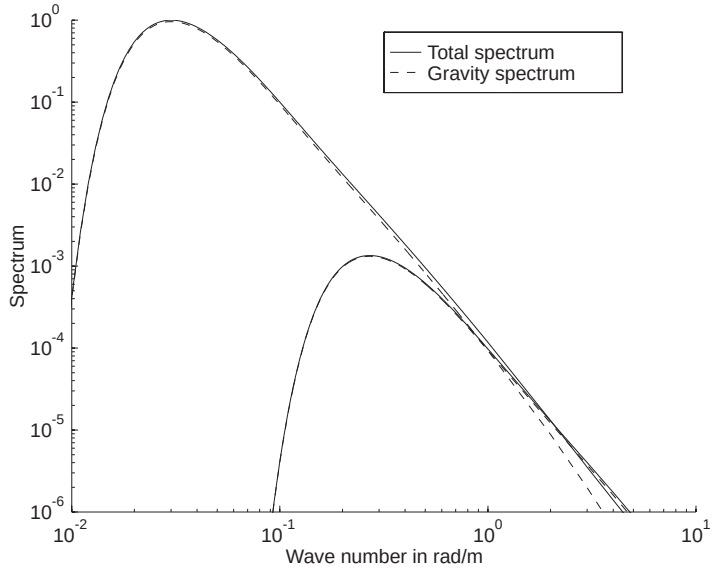

Figure 3. Isotropic part of the sea height spectrum versus the wave number. The wind speed $u_{10} = \{5, 15\}$ m/s. In full curve the total height spectrum (low- and high- wavenumbers) $k^{-3}(B_L + B_H)$, and in dashed curve the gravity height spectrum $k^{-3}B_L$ (low-wavenumber).

zone is responsible for Bragg backscattering, since the backscattering coefficient is equal to [2] $|B_{V,H}|^2 \cot^4(\theta)[B_L(2k_0) + B_H(2k_0)]/2$ ($k_0 = k \sin\theta$ and $\{B_{V,H}\}$ are expressed from (8a)). As shown Figure 5, the anisotropic effect increases in capillary region with the wind speed.

3.2. Surface Height and Slope Variances

In this subsection, the surface slope variances in upwind σ_x^2 and crosswind σ_y^2 directions are computed from the previous spectrum, with the aim to compare them with the Cox and Munk model [27]. From equation (4), the comparison of the rms surface slopes σ_X in the wind direction with the incident beam slope $\cot\theta$ allows to quantify the contribution of the $\{\chi_{1,2}\}$ additional terms provided by the Kirchhoff approximation.

From the general behavior of the directional sea spectrum, $\{\sigma_x^2, \sigma_y^2\}$ can be expressed as [21]

$$\sigma_x^2 = \alpha + \beta \quad \sigma_y^2 = \alpha - \beta \tag{20}$$

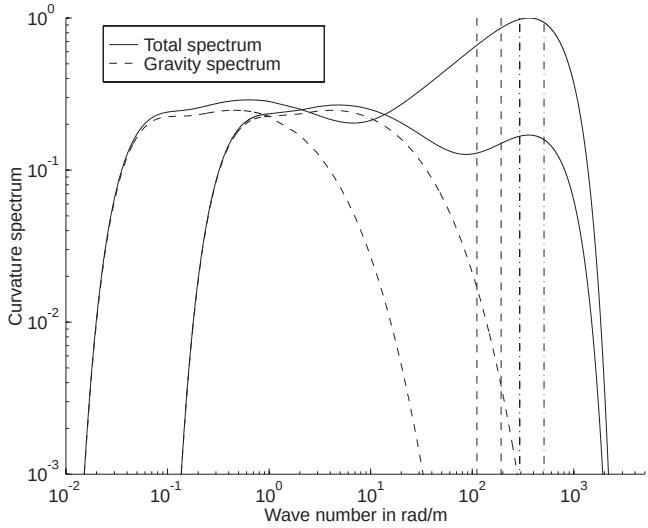

Figure 4. Isotropic part of the curvature sea spectrum versus the wave number. The wind speed $u_{10} = \{5, 15\}$ m/s. In full curve the total curvature spectrum (low- and high- wavenumber) $B_L + B_H$, and in dashed curve the curvature gravity B_L (low-wavenumber).

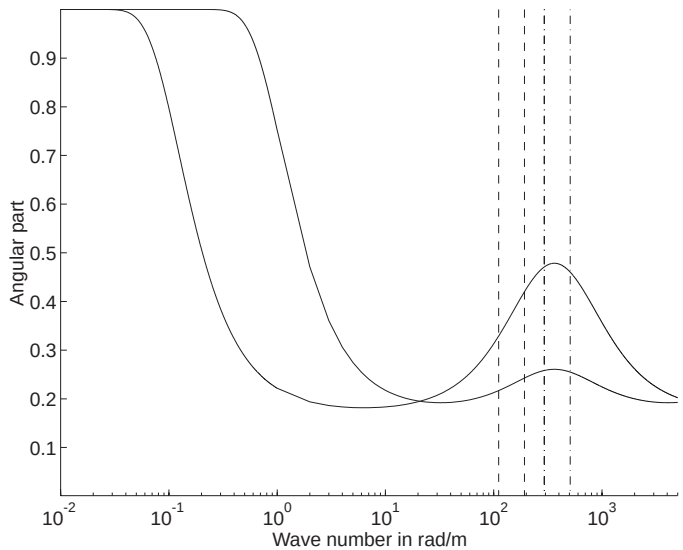

Figure 5. Angular part $\Delta(k)$ of the sea height spectrum versus the wave number. The wind speed $u_{10} = \{5, 15\}$ m/s.

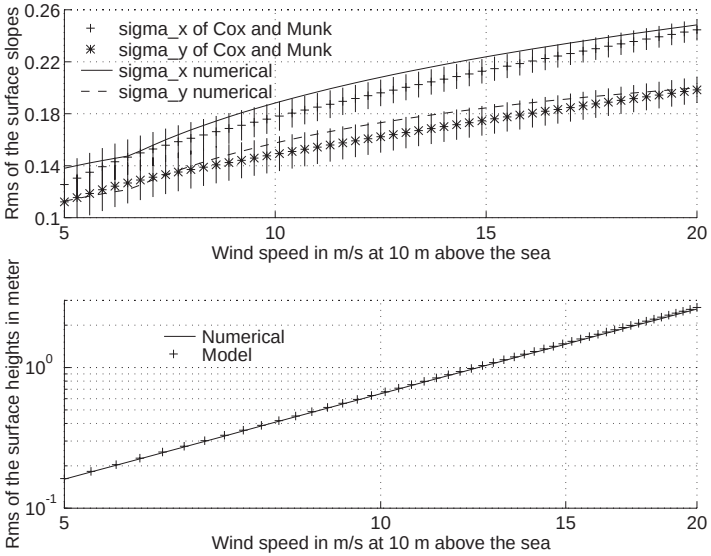

Figure 6. At the top, rms surface slopes in upwind σ_x, and crosswind directions σ_y obtained from the Cox-Munk data and computed from the Elfouhaily spectrum versus the wind speed u_{10} in m/s defined at ten meters above the sea. At the bottom, numerical and model rms surface heights versus u_{10}.

where

$$\begin{aligned} \alpha &= \tfrac{1}{2}\int_0^\infty k^{-1}[B_L(k)+B_H(k)]dk \\ \beta &= \tfrac{1}{4}\int_0^\infty k^{-1}[B_L(k)+B_H(k)]\Delta(k)dk \end{aligned} \tag{20a}$$

and for a Gaussian process, the surface slope variance $\sigma_X^2(\phi)$ in the wind direction ϕ is

$$\sigma_X^2(\phi) = \alpha + \beta\cos(2\phi) \tag{21}$$

We can notice that $\sigma_X^2(0) = \sigma_x^2$ and $\sigma_X^2(\pi/2) = \sigma_y^2$.

The Cox and Munk model gives

$$\sigma_x^2 = (3,16u_{12} \pm 4)10^{-3} \quad \sigma_y^2 = (3+1,92u_{12} \pm 4)10^{-3} \tag{22}$$

At the top of Figure 6, the rms surface slopes in upwind σ_x and crosswind directions σ_y obtained from the Cox-Munk model and computed from the Elfouhaily spectrum are plotted versus the wind speed u_{10} in m/s defined at ten meters above the sea. As depicted Figure 6, the Elfouhaily results which are slightly overestimated are in agreement with the Cox and Munk ones.

From the spectrum, the surface height variance ω^2 is defined as

$$\omega^2 = \int_0^\infty k^{-3}[B_L(k) + B_H(k)]dk \tag{23}$$

At the bottom of Figure 6, numerical and model [21] ($\omega^2 \approx 193 \times 10^{-5}/k_p^2 \approx 3,95 \times 10^{-5} u_{10}^{4,04}$ for a fully developed sea $\Omega = 0.84$) rms surface heights are represented versus u_{10}. A good fit is observed, and therefore ω is proportional to the square of the wind speed u_{10}. As depicted Figure 3, ω^2 is not affected by the capillarity waves permitting to model ω^2 with respect to k_p^2.

At the top and at the middle of Figure 7, the products $\sigma_x \tan(\theta)$ and $\omega \cos\theta$ are plotted versus u_{10}, respectively, for scattering angles $\theta = \{10, 30, 50, 60\}^\circ$ of interest for remote sensing. For scattering angles smaller than 60°, we can see that the product $\sigma_x \tan(\theta)$ is smaller than one ($u_{10} \in [5; 20]$ m/s). For wind speed u_{10} shorter than 10 m/s, the contribution in (4) of the $(\sigma_X \tan\theta)^2$ becomes then negligible. We can note that SSA is valid if the incident beam slope $1/\tan\theta$ is larger than the rms of the surface slopes which is similar to have $\sigma_X \tan\theta < 1$.

In the range frequencies $f \in [1; 20]$ GHz, $K \in [21; 419]$ rad/m. As depicted at the middle of Figure 7, for moderate scattering angles, the product $K_\omega = 2K\omega\cos\theta$ increases with the wind speed and can be larger than one. In (4), (6) and (8), the exponential term exp[...] becomes then small, and for the integration over radial distance r, the surface height normalized autocorrelation function can be replaced by its Taylor development of order two, which gives the optics geometrical approximation. For example, in C band ($f = 5.3$ GHz), $K = 111$ rad/m, $2K\omega\cos\theta \in [18; 592]$ with $u_{10} \in [5; 20]$ m/s and $\theta \in [0; 60]^\circ$. In Ku band ($f = 14$ GHz), the previous ranges are multiplied by 2.64, whereas in L band ($f = 1.5$ GHz), they are divided by 3.53.

3.3. Sea Surface Height Autocorrelation Function

In cartesian coordinates, the surface height autocorrelation function $R_0(x, y)$ is equal to the Fourier transform of the spectrum $\Psi(k_x; k_y)$. From (12) general behavior, in polar coordinates, the sea autocorrelation function $R_0(r, \Phi)$ is expressed from the sea spectrum $S(k, \psi) = k \times \Psi(k, \psi)$ as [21]

$$R_0(r, \Phi) = R_{00}(r) - \cos(2\Phi) R_{02}(r) \tag{24}$$

where

$$\begin{cases} R_{00}(r) = \displaystyle\int_0^\infty M(k) J_0(rk) dk \\ R_{02}(r) = \displaystyle\int_0^\infty M(k) \Delta(k) J_2(rk) dk \end{cases} \tag{25}$$

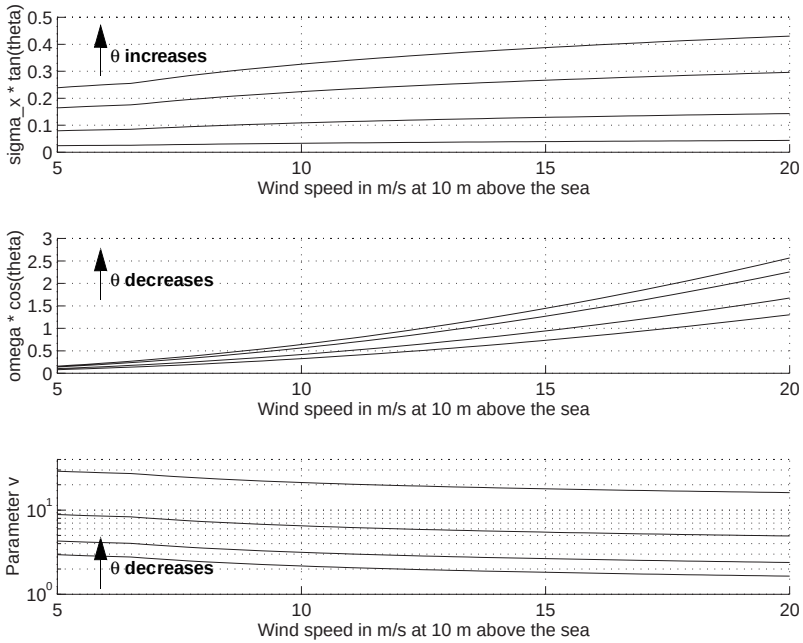

Figure 7. At the top, product $\sigma_x \tan(\theta)$ versus u_{10}. At the middle, product $\omega \cos\theta$ versus u_{10}. At the bottom, parameter $v = 1/(\sigma_x \tan(\theta)\sqrt{2})$ versus u_{10}. For three figures, the scattering angle $\theta = \{10, 30, 50, 60\}^\circ$.

$R_{00}(r)$ is the isotropic part, whereas $R_{02}(r)$ denotes the anisotropic part. J_n is the n^{th} order Bessel function of the first kind. Unlike Funk et al [4], the integration over ψ is performed analytically involving a dependence in $\cos(2\Phi)$. As the sea spectrum, the autocorrelation function is both even with respect to the upwind and crosswind directions.

From simulations with $u_{10} \in [2; 17]$ m/s, $R_0(r, \Phi)$ can be modeled as [21]

$$\begin{cases} R_{00}(r) = \omega^2 \cos\left(\dfrac{r}{L_0'}\right) / \left[1 + \left(\dfrac{r}{L_0}\right)^2\right] \\ R_{02}(r) = \omega^2 A J_2\left(\dfrac{r}{L_2'}\right) / \left[1 + \left(\dfrac{r}{L_2}\right)^2\right] \end{cases} \tag{26}$$

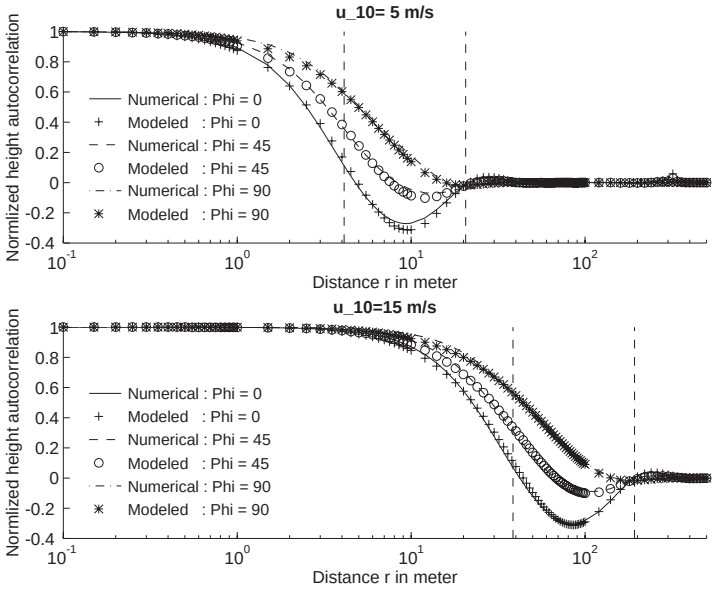

Figure 8. Comparison of the modeled surface normalized height autocorrelation function with the numerical one for wind directions $\Phi = \{0, 45, 90\}^\circ$ and wind speeds $u_{10} = \{5, 15\}$ m/s.

where

$$\begin{cases} \omega^2 = 3,953 \times 10^{-5} u_{10}^{4,04} & L_0 = 0,154 u_{10}^{2,04} & L_0' = 0,244 u_{10}^{1,91} \\ A = 3,439 u_{10}^{0,11} & L_2 = 0,157 u_{10}^{1,95} & L_2' = 0,138 u_{10}^{2,05} \end{cases} \tag{26a}$$

Figure 8 Compares the modeled surface normalized height autocorrelation function (equation (26)) with the numerical one ((equation (25)) versus the radial distance r for wind directions $\Phi = \{0, 45, 90\}^\circ$ and wind speeds $u_{10} = \{5, 15\}$ m/s. A good fit is observed between the numerical and modeled results. The vertical dashed lines are located at distance r corresponding to $L_0 = 0,154 u_{10}^{2,04}$ and $5L_0$. Note that the correlation length L_C increases very quickly with the wind speed and there is a significant range of negative values not present in most correlation functions for land surfaces. The correlation length can not be equal to L_0 since with respect to the wind direction, the autocorrelation function can be close to one (0.6 with $\Phi = 90^\circ$). On the other hand, for $r = 5L_0$ the autocorrelation function is close to zero which allows to take $L_C = 5L_0$. For $u_{10} = \{5, 15\}$ m/s, we have $L_C = \{20, 192\}$ meters.

The negative values of the autocorrelation function comes from the fact that the sea gravity spectrum reaches a maxima located around of k_p. This means that the sea spectrum can be expressed as a convolution product of a Dirac distribution centered around k_p by the spectrum centered in zero. The autocorrelation function is then equal to the product of the Fourier transforms of the sea spectrum and the Dirac function which explains the oscillatory behavior of $R_0(r, \Phi)$.

The computation of the backscattering coefficient with the Kirchhoff approximation requires also the knowledge of $\{R_{10}, R_{12}, R_{20}, R_{22}\}$ defined as $R_{ij} = d^i R_{0j}/dr^i$ (see equation (5a)). From (25), we can write

$$\begin{cases} R_{10} = \dfrac{dR_{00}}{dr} = -\displaystyle\int_0^\infty kM(k)J_1(rk)dk \\ R_{12} = \dfrac{dR_{02}}{dr} = \dfrac{1}{2}\displaystyle\int_0^\infty kM(k)\Delta(k)[J_1(rk) - J_3(rk)]dk \end{cases} \tag{27}$$

and

$$\begin{cases} R_{20} = \dfrac{d^2R_{00}}{dr^2} = -\dfrac{1}{2}\displaystyle\int_0^\infty k^2M(k)[J_0(rk) - J_2(rk)]dk \\ R_{22} = \dfrac{d^2R_{02}}{dr} = \dfrac{1}{4}\displaystyle\int_0^\infty k^2M(k)\Delta(k)[J_0(rk) - 2J_2(rk) + J_4(rk)]dk \end{cases} \tag{28}$$

The surface slope variance $\sigma_X^2(\phi)$ in the wind direction is defined as $-R_2(0, \phi) = -[R_{20}(0) - \cos(2\phi)R_{22}(0)]$. Comparing then (20a)–(21) with (28) and knowing that $\{J_0(0) = 1, J_{2,4}(0) = 0\}$, the same relationship is found.

Figure 9 compares the modeled isotropic $\{f_{10} = -R_{10}/(\omega\sigma_X), f_{20} = -R_{20}/(\omega\sigma_X)\}$ (on the left) and anisotropic $\{f_{12} = -R_{12}/\sigma_X^2, f_{22} = -R_{22}/\sigma_X^2\}$ (on the right) parts with the numerical ones for wind speeds $u_{10} = \{5, 15\}$ m/s. σ_X is chosen equal to α (wind direction equal to 45 degrees), ω is computed from (26a) and the modeled isotropic and anisotropic parts are provided by [20, table 2.5]. As depicted Figure 9, there is a discrepancy between the numerical and modeled results, because in (25) modeling of the surface height autocorrelation function $R_0(r, \Phi)$, the capillary region is omitted due to the attenuation in k^{-3} according to $S(k)$ (see Figure 3 with (12)). With the first and second derivatives of $R_0(r, \Phi)$ expressed from (27)–(28), this attenuation becomes $\{k^{-2}, k^{-1}\}$, respectively, which involves that the capillary region can not be ignored. We can also explain this deviation by the fact that there are several functions which can be modeled $R_0(r, \Phi)$ with very different derivatives.

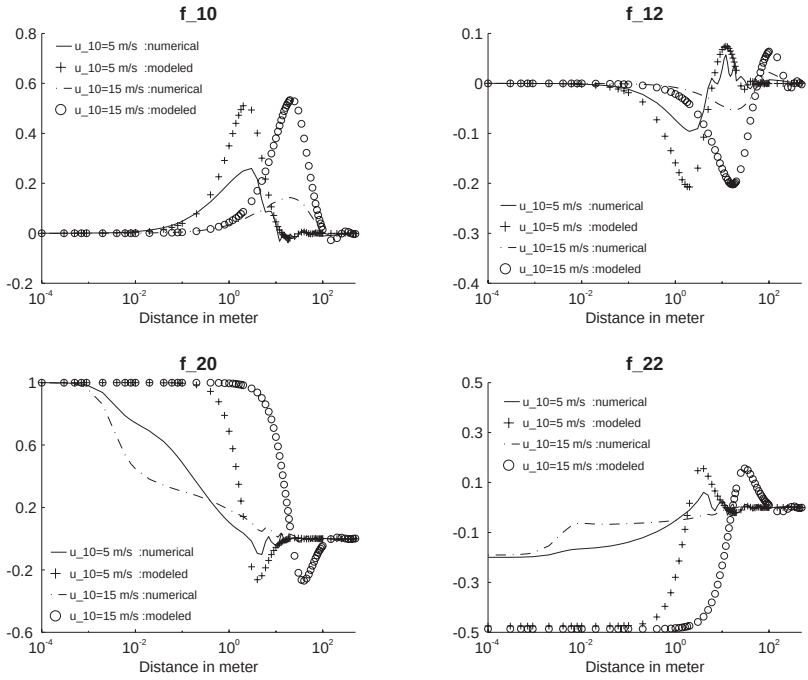

Figure 9. Comparison of the modeled isotropic $\{f_{10}, f_{20}\}$ (on the left) and anisotropic $\{f_{12}, f_{22}\}$ (on the right) parts with the numerical ones for wind speeds $u_{10} = \{5, 15\}$ m/s.

For the computation of the backscattering coefficient, the modeling of $R_0(r, \Phi)$ can be used, and the computations of its first and second derivatives have to be obtained from numerical evaluations of (27)–(28).

3.4. Shadowing Function

For a backscattering configuration, the shadowing function characterizes the surface fraction which is visible from the receiver. A study regarding the shadowing function has been done with Smith [33, 34] and Wagner [35]. These authors determined the shadowing function for a one-dimensional stationary stochastic process. Bourlier et al [20, 36] extended their results for a two-dimensional stationary surface by including the correlation between the surface heights and slopes. They also noted that Smith's results are more accurate than Wagner's. Since the difference between the correlated and uncorrelated Smith's shadowing functions is very small, the uncorrelated statistical shadowing

function can be used with a good approximation.

As shown Bourlier et al [18, 19], for a scattering problem, the shadowing function modifies the height distribution and carries a restriction over the surface slopes. With the Smith formulation, the surface joint height and slope distribution with shadow $p_{Sh}(\zeta_X, h)$ is then written as [18]

$$p_{Sh}(h, \zeta_X) = p(h, \zeta_X) \times \Upsilon(v - \zeta_X) \left[1 - \frac{1}{2}\mathrm{erfc}(h)\right]^{\Lambda(v)} \tag{29}$$

where $p(\zeta_X, h)$ is the unshadowed distribution assumed to be Gaussian

$$p(h, \zeta_X) = \exp(-\zeta_X^2 - h^2)/\pi \tag{29a}$$

ζ_X is the surface slope normalized by $\sigma_X\sqrt{2}$ (σ_X given by (21)), and h the surface elevation normalized by $\omega\sqrt{2}$. In (29)

$$\Lambda(v) = [\exp(v^2) - v\sqrt{\pi}\mathrm{erfc}(v)]/(2v\sqrt{\pi}) \quad v = \cot\theta/(\sqrt{2}\sigma_X) \tag{29b}$$

$$\Upsilon(x) = 1 \quad \text{if } x \geq 0 \quad \text{else } 0 \tag{29c}$$

where $\Upsilon(x)$ is the Heaviside function. The shadowing function involves therefore a restriction over the surface slopes within the term $\Upsilon(v-\zeta_X)$, and modifies the height distribution due to the term, $[1-\mathrm{erfc}(h)/2]^{\Lambda(v)}$.

In Figure 10, the shadowed surface slope ($p_{Sh}(\zeta_X) = p(\zeta_X)\Upsilon(v - \zeta_X)$ term of (29) plotted on the left) and height ($p_{Sh}(h) = p(h)[1 - \mathrm{erfc}(h)/2]^{\Lambda(v)}$ term of (29) plotted on the right) distributions are compared with the unshadowed one (crosses curve) according to the parameter v and versus the normalized slope ζ_X and height h. We see that the area of $p_{Sh}(\zeta_X)$ is inversely proportional of v and for $v = 0$, only the negative values of $p_{Sh}(\zeta_X)$ are taken into account. Since $p(\zeta_X = 2) = 0.01$, for v larger than 2 the shadowing effect on the surface slopes is negligible. As depicted in Figure 10 (right), the shadowing effect on the surface height distribution increases when v decreases due to the fact that (29b) Λ increases, and for $v \geq 2$, the shadowing effect can be ignored.

In conclusion, if $v \geq 2$, then the shadowing effect on the surface heights and slopes can be omitted and $p_{Sh}(h, \zeta_X) \approx p(h, \zeta_X)$.

At the bottom of Figure 7, the parameter $v = 1/(\sigma_x \tan\theta\sqrt{2})$ is plotted versus u_{10}, with scattering angles $\theta = \{10, 30, 50, 60\}^\circ$. Since v is greater than 1.6, the shadowing effect can be neglected for the computation of the backscattering coefficient. This result is in agreement with articles [18, 19] which explains how the shadowing function can be accounted for the Kirchhoff approximation. As proved

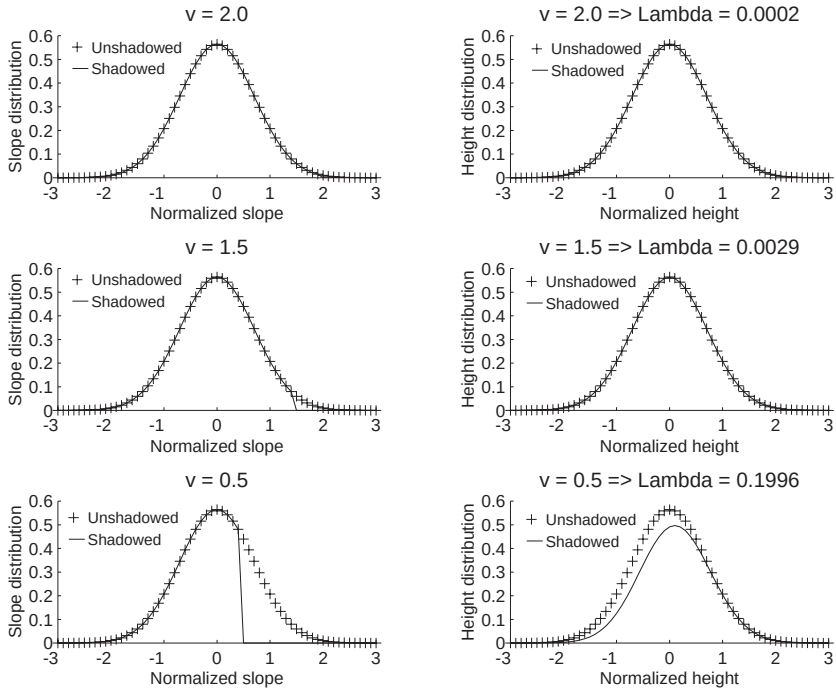

Figure 10. Comparison of the shadowed and unshadowed distributions of the surface slopes (left) and heights (right) according to the parameter v and versus the normalized surface slopes ζ_X and heights h.

by Sancer [37], with the geometrical optics approximation, the average shadowing function (integrations over $\{h, \zeta_X\}$ of (29)) can be used and it is equal to $S(v) = [1 + \text{erfc}(v)]/\{2[1 + \Lambda(v)]\}$. Then $S(1.6) = 0.986$.

4. NUMERICAL RESULTS

In this section, the incoherent backscattering models presented in Section 2 are computed from the sea directional spectrum given in Section 3. To compare the Kirchhoff approach (KA) with the small slope approximation (SSA), in the first subsection, the sea surface is assumed to be perfectly conducting with an isotropic spectrum. In Subsection 2, the models are compared for a dielectric sea surface, and in Subsection 3, the effect of the wind direction is analyzed within the CMOD2-I3 and SASS-II backscattering models valid in C and Ku bands, respectively.

4.1. Perfectly-Conducting Surface with an Isotropic Sea Spectrum

For an isotropic surface, the anisotropic part of the sea surface spectrum is equal to zero involving in (12b) that $\Delta(k) = 0$ and the spectrum depends only on the wave number k. This means from (5a), $\{R_{i2}\} = 0$, $\sigma_X = \sigma_Y = \sigma_x)$, and from (5b), $\{C_{16}, C_{36}\} = 0$, $C_{56} = R_{10}/r$. The $\{\chi_1, \chi_2\}$ terms of (4b)–(4c) becomes then

$$\chi_1 = 2K_\omega \times cf_1 \quad \chi_2 = c^2 f_2 + s^2 f_{56} - K_\omega^2 (cf_1)^2 \tag{29d}$$

We can also notice that $f_i = f_{i0}$.

Knowing that

$$\Psi_0 = \int_0^{2\pi} \exp[jx\cos(\phi - \Phi)]d\Phi = 2\pi J_0(x) \tag{30}$$

we have

$$\left\{ \begin{array}{l} \Psi_1 = \displaystyle\int_0^{2\pi} \cos(\phi - \Phi) \times \exp[jx\cos(\phi - \Phi)]d\Phi \\ \quad = -j\dfrac{\partial \Psi_0}{\partial x} = 2\pi j J_1(x) \\ \Psi_2 = \displaystyle\int_0^{2\pi} [\cos(\phi - \Phi)]^2 \times \exp[jx\cos(\phi - \Phi)]d\Phi \\ \quad = -j\dfrac{\partial \Psi_1}{\partial x} = \pi[J_0(x) + J_2(x)] \\ \Psi_3 = \displaystyle\int_0^{2\pi} \cos[2(\phi - \Phi)] \times \exp[jx\cos(\phi - \Phi)]d\Phi \\ \quad = 2\Psi_2 - \Psi_0 = -2\pi J_2(x) \end{array} \right. \tag{30a}$$

Substituting (29d) into (4), we show with the use of (30a) that the integration over Φ of (3) incoherent backscattering coefficient with the Kirchhoff approximation leads to

$$\begin{aligned} \sigma^{KA} \;=\; & 2(K\cos\theta)^2 \exp(-K_\omega^2) \int_0^\infty \Big(\exp(K_\omega^2 f_0)\{J_0(xr) \\ & \cdot[1 + (\sigma_X \tan\theta)^2 (f_2 + f_{56} - f_1^2 K_\omega^2)/2] \\ & -2J_1(xr)(\sigma_X \tan\theta) f_1 K_\omega - J_2(xr)(\sigma_X \tan\theta)^2 \\ & \cdot(f_2 - f_{56} - f_1^2 K_\omega^2)/2\} - J_0(xr)\Big) r dr \end{aligned} \tag{31}$$

where

$$x = 2K\sin(\theta) \tag{31a}$$

With the stationary phase (SP) method, the incoherent backscattering coefficient is from (7)

$$\sigma^{SP} = 2(K/\cos\theta)^2 \exp(-K_\omega^2)|R_{H,V}|^2 \int_0^\infty r J_0(xr)[\exp(K_\omega^2 f_0) - 1]dr \tag{32}$$

with $R_V = 1$ and $R_H = -1$ for a perfectly conducting. For a sufficiently rough surface ($K_\omega \gg 1$), the geometrical optics approximation (exponent GO) or high-frequency limit is obtained by approximating f_0 by the first two terms of its Taylor series expansion about the origin. The integration over r of (32) leads to

$$\sigma^{GO} = |R_{H,V}|^2 \exp[-\tan^2\theta/(2\sigma_x^2)]/(2\sigma_x^2\cos^4\theta) \tag{33}$$

For the small slope approximation, the incoherent backscattering coefficient σ^{SSA} required the computation of (11) modified surface height autocorrelation $f_{0M}(r,\Phi)$. From (9b)–(9c) and (11a), $\Xi_{V,H} = 1 - B_{1V,1H}(\xi,\psi)/(2K\cos\theta)$ can be written as

$$\begin{cases} \Xi_V = 1 + \dfrac{K^2[\xi^2\cos^2(\psi-\phi) - \xi^2 + K^2] - k_0^2[\xi^2 + 2\xi k_0\cos(\psi-\phi) + k_0^2]}{[K^2 - \xi^2 - k_0^2 - 2k_0\xi\cos(\psi-\phi)]^{1/2}(K^2-k_0^2)^{1/2}(K^2+k_0^2)} \\ \Xi_H = 1 + \dfrac{K^2 - [\xi\cos(\psi-\phi) + k_0]^2}{[K^2 - \xi^2 - k_0^2 - 2k_0\xi\cos(\psi-\phi)]^{1/2}(K^2-k_0^2)^{1/2}} \end{cases} \tag{34}$$

We can note for $\xi = 0$, the above equations are equal to 2. Although the sea spectrum is assumed to be isotropic, the integration over ψ of (11) can not be performed analytically. Substituting (11) into (8), and using (3), the normal radar cross section with the small slope approximation (exponent SSA) is

$$\begin{aligned} \sigma_{SSA} \;=\; & \frac{(K\cos\theta)^2\exp(-K_\omega^2)|B_{H,V}|^2}{\pi} \\ & \cdot \int_0^\infty r dr \int_0^{2\pi} \exp[2jrK\sin(\theta)\cos(\Phi-\phi)] \\ & \cdot \Bigg(\exp\left\{ \frac{K_\omega^2}{8\pi\omega^2} \int_0^\infty M(\xi)d\xi \int_0^{2\pi} |\Xi(\xi,\psi-\phi)|^2 \right. \\ & \left. \cdot \exp[j\xi r\cos(\psi-\Phi)]d\psi \right\} - 1 \Bigg) d\Phi \end{aligned} \tag{35}$$

For given wind direction ϕ and $k_0 = K\sin\theta$, the computation of σ^{SSA} requires therefore four-fold integrations over $\{\psi, \xi, \Phi, r\}$ demanding an extensive computer time.

For an isotropic surface, we have $S(\xi,\psi) = M(\xi)/(2\pi)$, and for a perfectly conducting $B_H = -1,\ B_V = -[\sin^2(\theta)+1]/\cos^2(\theta)$ which are equal to the polarization terms of the small perturbation method [2].

The first-order SSA solution (exponent SSA0) is obtained when in (34), $\xi = 0$ meaning that $\{\Xi_{V,H}\} = 2$. Substituting these relationships into (35), the integration over ψ leads to $8\pi J_0(\xi r)$. The integration over ξ corresponds then to the isotropic part of the surface height autocorrelation function $R_{00}(r)$ (see equation (25)). Performing the integration over Φ, we obtain finally the same form as with the stationary method

$$\sigma^{SSA0} = 2(K\cos\theta)^2|B_{H,V}|^2\exp(-K_\omega^2)\int_0^\infty rJ_0(xr)[\exp(K_\omega^2 f_0)-1]dr \tag{36}$$

The comparison of (36) with (32) yields $\sigma^{SSA0} = \sigma^{SP}(\cos\theta)^4|B_{H,V}/R_{H,V}|^2$.

Approximating (34) $|\Xi_{V,H}|^2$ by the first term of its Taylor series expansion about the origin $\xi = 0$, and applying the same way as previously, we show in appendix A

$$\begin{aligned}\sigma^{SSA1} \;=\; & 2(K\cos\theta)^2|B_{H,V}|^2\exp(-K_\omega^2)\int_0^\infty\{\exp(K_\omega^2 f_{00}) \\ & \cdot J_0(xr - K_\omega^2 f_{10}\sigma_x/[\omega K_{V,H}]) - J_0(xr)\}rdr\end{aligned} \tag{37}$$

where $\{f_{00} = f_0, f_{10} = f_1\}$ (isotropic surface) and $\{K_{V,H}\}$ are defined from (A5).

In the numerical examples presented in this section, the isotropic wavenumber spectrum of Section 3.1 for a fully developed sea with $\Omega = 0.84$ is assumed.

Figure 11 presents predictions of (31) σ^{KA} Kirchhoff approximation (full curve), (32) σ^{SP} phase stationary (chain curve) and (33) σ^{OG} optics geometric scattering (circle curve) normal radar cross sections. Also shown in this figure are the predictions of small slope approximation term (36) of σ^{SSA0} (symbols plus) and the small perturbation method (symbols x-marks). Only the HH polarization case is depicted (the VV case is discussed later for a dielectric surface). At the top and at the bottom of Figure 11, the NRCS is plotted for C ($f = 5.3\,\mathrm{GHz}$) and Ku bands ($f = 14\,\mathrm{GHz}$), respectively, with wind speeds $u_{10} = \{5, 15\}$ m/s.

At near-nadir scattering angles, the KA, SP, SSA0 models are similar, whereas the OG solution is overestimated by several dB. As discussed [11, 14], the deviation come from the fact that the wave spectral components $k > 2K$ may contribute significantly to the RMS

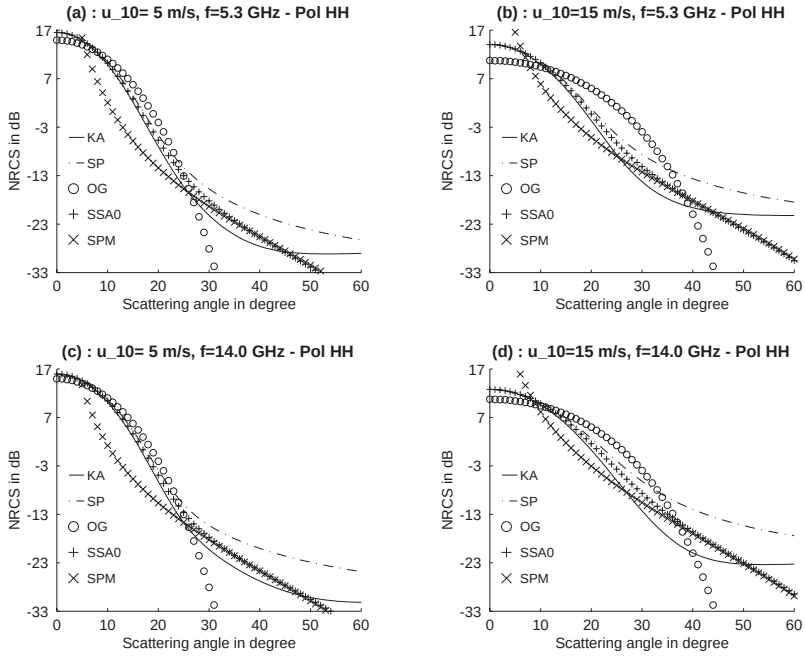

Figure 11. HH normal radar cross section in C ($f = 5.3\,\mathrm{GHz}$, at the top) and Ku Bands ($f = 14\,\mathrm{GHz}$, at the bottom) versus the scattering angle for wind speeds $u_{10} = \{5, 15\}\,\mathrm{m/s}$ with an isotropic sea surface assumed to be perfectly conducting. Kirchhoff approximation σ^{KA} in full curve, stationary phase σ^{SP} in chain curve, optics geometric σ^{OG} in circle curve, first-order small slope approximation σ^{SSA0} in symbols plus, and the small perturbation method in symbols x-marks.

slope but contribute negligibly to scattering. A smooth transition at scattering angles of 20–40 degrees where the geometric-optics regime becomes not valid and where the Bragg scattering regime predominates is observed. In this region, the deviation between the KA and SSA0 models increases with the scattering angle, and the SP results are underestimated. In fact with KA, there are numerical problems for large incidence angles. Since for the HH polarization, $B_H = -1$, we get $\sigma^{SP} = \sigma^{SSA0}/(\cos\theta)^4$ with explains the overprediction of SP.

Figure 12 compares the SSA0 results with (37) SSA1 ones for VV and HH polarizations with the same parameters as Figure 11. Unlike with the Kirchhoff approach, for a perfectly-conducting surface, the SSA model for the VV polarization is larger than the HH one because the polarization terms $\{B_{V,H}\}$ are different. We can also see that

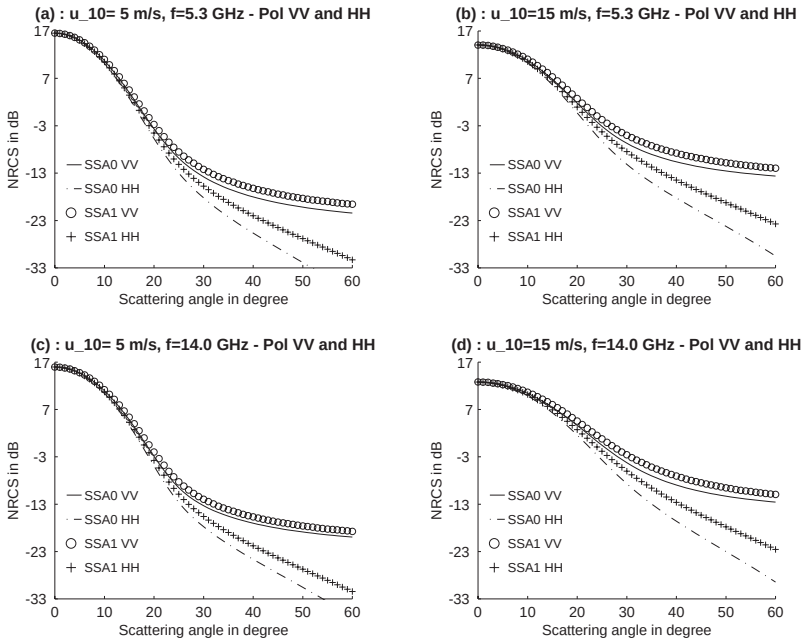

Figure 12. Comparison of the SSA0 results with SSA1 ones for VV and HH polarizations with the same parameters as Figure 11.

the discrepancy between the SSA0 and SSA1 models increases with the scattering angle, involving that the SSA1 model is not similar to the rigorous SSA solution. This solution will be discussed for a two-dimensional dielectric surface.

When the isotropic part of (26) sea surface height modeled autocorrelation function $R_{00}(r)$ is used, the NRCS is very different than the one computed from (25). Therefore, for the simulations $R_{00}(r)$ is computed numerically from (25). This explains by the fact that around zero, $R_{00}(r)$ has to be very accurate for observing the Bragg regime.

4.2. Dielectric Surface with an Isotropic Sea Spectrum

As shown Bourlier et al [18], for a dielectric surface, the integrand in the Kirchhoff integral is a very complicated function involving that the integrations over the statistical variables (heights and slopes) can not be performed analytically. On the other hand, the SA model presented in this subsection can be used.

Using the same way as previously, the incoherent backscattering

coefficient under the scalar approximation σ^{SA} is from (6)

$$\begin{aligned}\sigma^{SA} &= 2(K\cos\theta)^2\exp(-K_\omega^2)|R_{H,V}|^2\int_0^\infty rdr\\ &\cdot\Big(\exp(K_\omega^2 f_0)\{J_0(xr)-2J_1(xr)(\sigma_X\tan\theta)f_1K_\omega\\ &\cdot\Re(R_{H,V}R_{H1,V1})/|R_{H,V}|^2-J_0(xr)\}\Big)\end{aligned} \tag{38}$$

For the SSA1 model, equation (37) is similar, where the $\{K_V, K_H\}$ are expressed from (9b)–(9c) (see appendix A) as

$$K_H = \Re\left[\frac{q_{01}^2 q_{02}}{k_0(q_{01}-q_{02})}\right] \tag{38a}$$

$$K_V = \Re\left\{\frac{K^2(q_{02}^2+\varepsilon_r k_0^2)q_{02}(k_0^2-K^2)(q_{01}q_{02}+k_0^2)}{k_0(q_{01}-q_{02})[q_{01}^3q_{02}^3+K^2k_0^4+k_0^2(q_{01}^3q_{02}-2\varepsilon_r K^4)]}\right\} \tag{38b}$$

where $\{q_{01}, q_{02}, k_0\}$ are given by (9d).

Figures 13–14 represents the NRCS of SA (full curve), SSA0 (chain curve), SP (circle curve), OG (plus curve) versus the scattering angle for VV and HH polarizations in C ($f = 5.3\,\mathrm{GHz}$, $\varepsilon_r = 67 + j35$ [28], at the top) and Ku Bands ($f = 14\,\mathrm{GHz}$, $\varepsilon_r = 47 + j38$ [28], at the bottom). The wind speeds $u_{10} = \{5, 15\}\,\mathrm{m/s}$.

For the HH polarization, since $R_H = B_H$, the deviation between the SA and SSA0 models is smaller than the one obtained for VV polarization. For the VV polarization, $|B_V| > |B_H|$ which explains in Figure 15 that the scattering coefficient in VV polarization is greater than the one computed for HH polarization. In fact we have $\sigma_{VV}^{SSA0}/\sigma_{HH}^{SSA0} = |B_H/B_V|^2$.

Voronovich [11, Figures 1-(e) and 1-(f)] have compared the SSA0 and (35) SSA models with the same parameters as (c)–(d) of Figure 15 ($f = 14\,\mathrm{GHz}$ and $u_{10} = \{5, 15\}\,\mathrm{m/s}$). He observed for scattering angles $\theta \in [0; 60]^\circ$ that the SSA0 and SSA scattering coefficients are similar for the VV polarization, whereas for the HH polarization, the difference $\sigma_{HH}^{SSA} - \sigma_{HH}^{SSA0} > 0$ increases with the wind speed, but remains within about 2 dB which is observed in Figure 15 with the σ_{HH}^{SSA1} model. Therefore, $\sigma^{SSA0} \approx \sigma_{SSA}$ with an accuracy of order 2 dB. McDaniel [14, Figures 4–5] with $u_{10} = \{5, 10\}\,\mathrm{m/s}$ and $f = 5.3\,\mathrm{GHz}$, observed a deviation $\sigma^{SSA} - \sigma^{SSA0} > 0$ less smaller than 0.8 dB. Therefore, the SSA1 model is not sufficient for the HH polarization to account for the SSA formulation. Nevertheless, $\sigma^{SSA0} \approx \sigma^{SSA}$ allowing to compute rapidely the backscattering coefficient, since the SSA requires four-fold integrations.

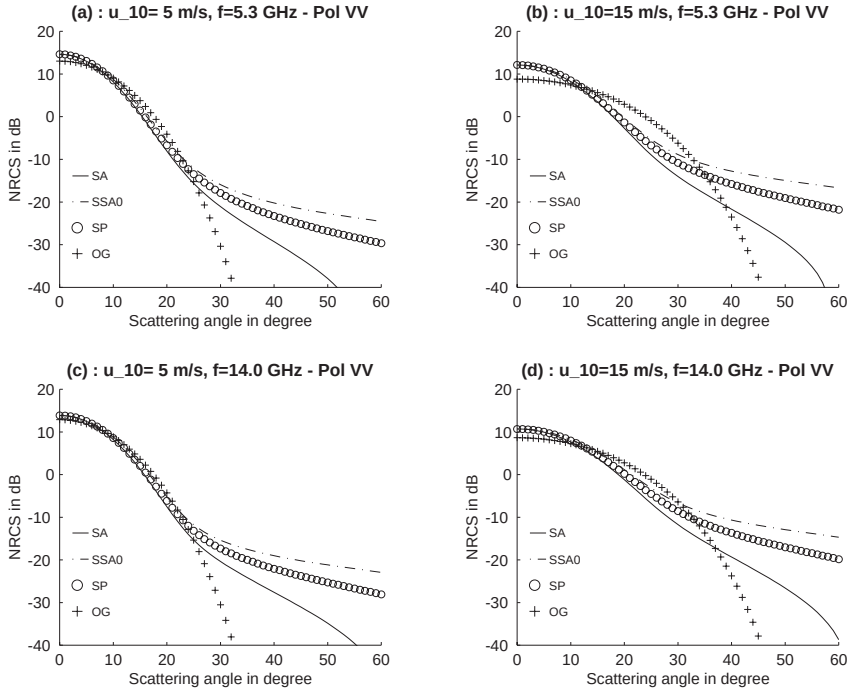

Figure 13. VV normal radar cross section in C ($f = 5.3\,\mathrm{GHz}$, $\varepsilon_r = 67 + j35$, at the top) and Ku Bands ($f = 14\,\mathrm{GHz}$, $\varepsilon_r = 47 + j38$, at the bottom) versus the scattering angle for wind speeds $u_{10} = \{5, 15\}$ m/s with a dielectric isotropic sea surface.

4.3. Dielectric Surface with an Anisotropic Sea Spectrum

From measurements made in microwave band [23–26] for co-polarizations pq (VV and HH), the NRCS is given as

$$\sigma_{pq} = \sigma^0_{pq} + \sigma^1_{pq}\cos\phi + \sigma^2_{pq}\cos(2\phi) \tag{39}$$

In (39), the mean backscatter σ^0_{pq} mainly carries the information of the wind speed, σ^1_{pq} describes the upwind and downwind asymmetry, and σ^2_{pq} accounts for the difference in backscatter extrema. We get

$$\begin{cases} \sigma^0_{pq} = (\sigma^u_{pq} + \sigma^d_{pq} + 2\sigma^c_{pq})/4 \\ \sigma^1_{pq} = (\sigma^u_{pq} - \sigma^d_{pq})/2 \\ \sigma^2_{pq} = (\sigma^u_{pq} + \sigma^d_{pq} - 2\sigma^c_{pq})/4 \end{cases} \tag{39a}$$

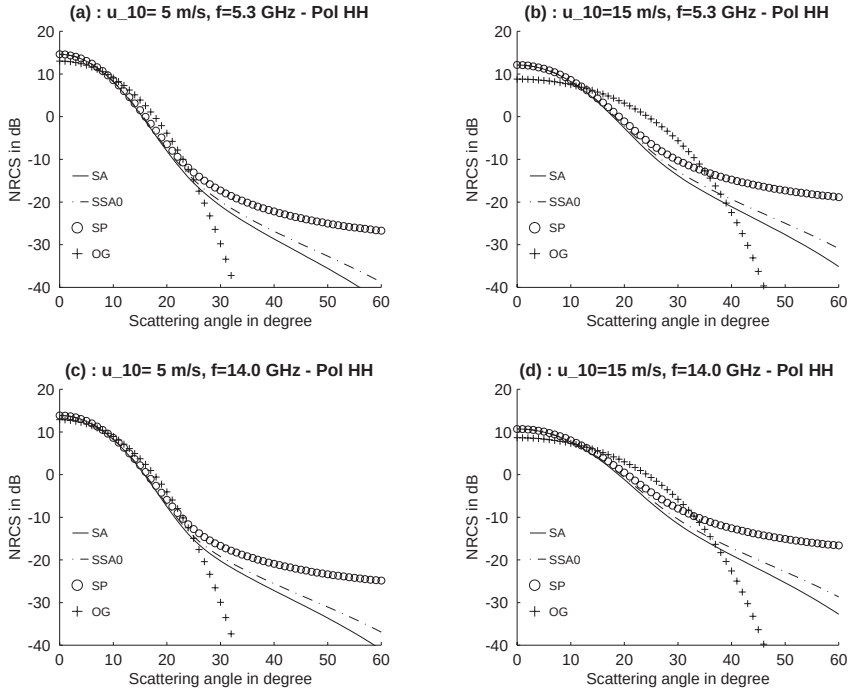

Figure 14. Same variation as Figure 13 for HH polarization.

where $\{\sigma_{pq}^u, \sigma_{pq}^c, \sigma_{pq}^d\}$ are the backscattering coefficients in upwind ($\phi = 0°$), crosswind ($\phi = 90°$) and downwind directions ($\phi = 180°$), respectively.

In paper [11, 14], the effect of the wind direction ϕ is studied numerically from the previous model. The originality of this subsection is to give an analytical representation of the $\{(\sigma_{pq}^{0,1,2}\}$ terms from the SSA0 and SA approaches.

For a two-dimensional sea surface, the general behavior of the sea surface height autocorrelation function $R_0(r, \Phi)$ is expressed as (24) $R_0(r, \Phi) = R_{00}(r) - \cos(2\Phi)R_{02}(r)$, where the isotropic $R_{00}(r)$ and anisotropic $R_{02}(r)$ parts are given by (25). Substituting these equations into (35), the integration over ψ yields then for the SSA0 approach ($|\Xi(\xi, \psi - \phi)| = 2$ which means $\xi = 0$)

$$\sigma^{SSA0} = \frac{(K\cos\theta)^2 \exp(-K_\omega^2)|B_{H,V}|^2}{\pi} \int_0^\infty r dr \int_0^{2\pi} \exp[jxr\cos(\Phi - \phi)] \cdot(\exp\{K_\omega^2[f_{00}(r) - \cos(2\Phi)f_{02}(r)]\} - 1)d\Phi \quad (40)$$

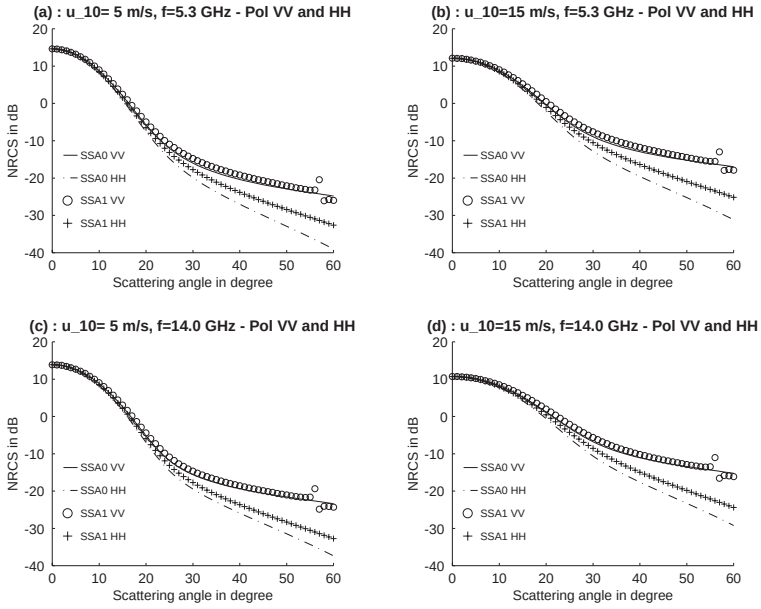

Figure 15. Comparison of the SSA0 model with SSA1 one for VV and HH polarizations. At the top $f = 5.3\,\mathrm{GHz}$, and at the bottom $f = 14\,\mathrm{GHz}$.

where x is given by (31a), $f_{00} = R_{00}/\omega^2$ and $f_{02} = R_{02}/\omega^2$. The use of (B4) leads to

$$\sigma^{SSA0} = 2(K\cos\theta)^2|B_{H,V}|^2 \int_0^\infty r dr \Bigg\{ \exp\{-K_\omega^2[1 - f_{00}(r)]\} \cdot \left[J_0(xr)I_0(x_1) + 2\sum_{n=1}^{\infty} \cos(2n\phi) J_{2n}(xr) I_n(x_1) \right] - J_0(xr)\exp(-K_\omega^2) \Bigg\} \tag{41}$$

with

$$x_1(r) = K_\omega^2 f_{02}(r) = (2K\omega\cos\theta)^2 f_{02}(r) \tag{41a}$$

with $\{J_n, I_n\}$ the n^{th}-order Bessel function of the first and second kinds, respectively.

In Figure 16, the $\exp\{-(2K\omega)^2[1 - f_{00}(r)]\} \times I_n[(2K\omega)^2 f_{02}(r)]$ ($x_1(r) = (2K\omega)^2 f_{02}(r)$ for $\theta = 0$) function is plotted versus the radial distance r for wind speeds $u_{10} = 5\,\mathrm{m/s}$ (at the top) and $u_{10} = 15\,\mathrm{m/s}$ (at the bottom) with frequencies $f = \{5.3, 14\}\,\mathrm{GHz}$. $n = \{0, 1, 2\}$. We

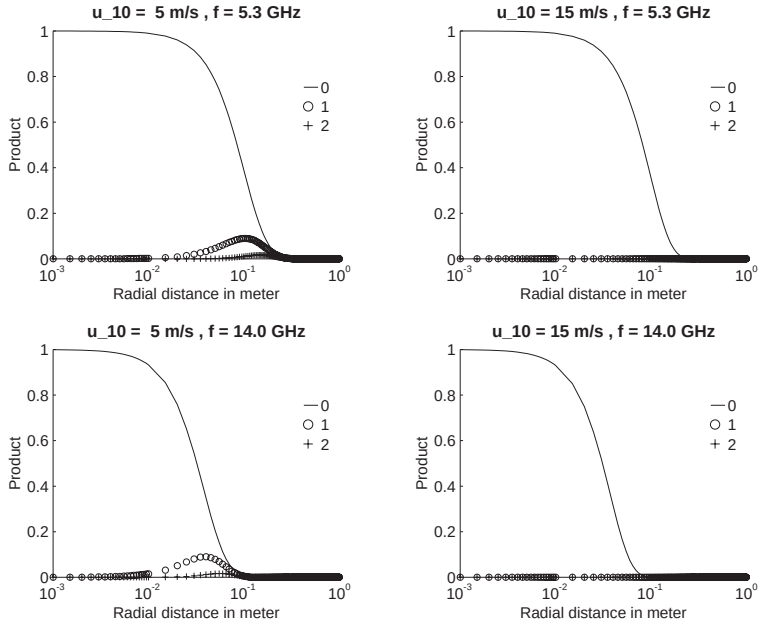

Figure 16. Variation of $\exp\{-(2K\omega)^2[1 - f_{00}(r)]\} \times I_n[K_\omega^2 f_{02}(r)]$ function versus the radial distance r for wind speeds $u_{10} = 5\,\mathrm{m/s}$ (at the top) and $u_{10} = 15\,\mathrm{m/s}$ (at the bottom) with frequencies $\{f = 5.3, 14\}\,\mathrm{GHz}$, $n = \{0, 1, 2\}$.

observe that the term of order $n = 2$ can be neglected. Moreover, in (41) around of zero, the $J_{2n\neq 0}(xr)$ functions with $x = 2K\sin\theta$ is close to zero which decreases the term in the symbol Σ. This involves that the backscattering coefficient can be written as (39) (the subscript pq is understood)

$$\sigma^{SSA0} = \sigma^{SSA0,0} + \sigma^{SSA0,1}\cos\phi + \sigma^{SSA0,2}\cos(2\phi) \tag{42}$$

where

$$\sigma^{SSA0,0} = 2(K\cos\theta)^2|B_{H,V}|^2\exp(-K_\omega^2) \cdot \int_0^\infty rJ_0(xr)[I_0(x_1)\exp(K_\omega^2 f_{00}) - 1] \tag{42a}$$

$$\sigma^{SSA0,1} = 0 \tag{42b}$$

$$\sigma^{SSA0,2} = 4(K\cos\theta)^2|B_{H,V}|^2\exp(-K_\omega^2)\int_0^\infty r\exp(K_\omega^2 f_{00})J_2(xr)I_1(x_1) \tag{42c}$$

If the surface is assumed to be isotropic,then $x_1 = 0$, meaning that $\{I_0(x_1), I_1(x_1)\} = \{1, 0\}$. $\sigma^{SSA0,2}$ is then equal to zero and $\sigma^{SSA0,0} = \sigma^{SSA0}$ (equation (36)). We can notice that $\sigma^{SSA0,1} = 0$ since the sea spectrum is assumed to be even in the upwind and crosswind directions due to the behavior in $\cos(2\Phi)$.

With the SSA model, Voronovich [11, Figures 2 and 4] showed in Ku and C bands for wind speeds $u_{10} = \{5, 10, 15\}$ m/s that the backscattering coefficient in the upwind and downwind directions coincide, involving from (39a) $\sigma^{SSA,1} = 0$. Therefore, although (11) modified autocorrelation function is not symmetrical, σ^{SSA} is symmetrical.

As discussed by Fung [39], the asymmetry of the radar cross section can be studied within the skewness effect. The sea spectrum is then represented by its real part which is centro-symmetric whereas its imaginary part is not equal to zero and it is an antisymmetric function. The spectrum is then Hermitian.

Substituting (4d), (5), (5a), (5b) into (4b), we get

$$\begin{aligned}\sigma_{X\chi 1} &= -4K\cos\theta \times \{\cos(\phi-\Phi)[R_{10} - \cos(2\Phi)R_{12}] \\ &\quad +2\sin(\phi-\Phi)R_{02}\sin(2\Phi)/r\} \end{aligned} \tag{43}$$

The use of (6) with (3) leads to

$$\begin{aligned}\sigma^{SA} &= \frac{(K\cos\theta)^2\exp(-K_\omega^2)|R_{H,V}|^2}{\pi} \\ &\quad \cdot\int_0^\infty r dr\int_0^{2\pi} d\Phi\langle\ldots\rangle^{SA}\exp[jxr\cos(\Phi-\phi)] \end{aligned} \tag{44}$$

where

$$\begin{aligned}\langle\ldots\rangle^{SA} &= \exp\{K_\omega^2[f_{00}(r) - \cos(2\Phi)f_{02}(r)]\} \\ &\quad \cdot\{1 - 4j\sin(\theta)K\Re(R_{H,V}R_{H1,V1})/|R_{H,V}|^2 \\ &\quad \cdot\{\cos(\phi-\Phi)[R_{10} - \cos(2\Phi)R_{12}] \\ &\quad +2\sin(\phi-\Phi)R_{02}\sin(2\Phi)/r\}\} - 1 \end{aligned} \tag{45}$$

where σ^{SA} is the incoherent backscattering coefficient under the scalar approximation (SA).

Substituting (45) into (44) and making the integration over Φ we show

$$\begin{aligned}\sigma^{SA} &= 2(K\cos\theta)^2\exp(-K_\omega^2)|R_{H,V}|^2\int_0^\infty\{\exp(K_\omega^2 f_{00}) \\ &\quad \cdot[C_0 - 4K\sin\theta\Re(R_{H,V}R_{H1,V1}) \\ &\quad \cdot(R_{10}C_1 - R_{12}C_2 + 2R_{02}S_2/r)/|R_{H,V}|^2] - J_0(xr)\}r dr \end{aligned} \tag{46}$$

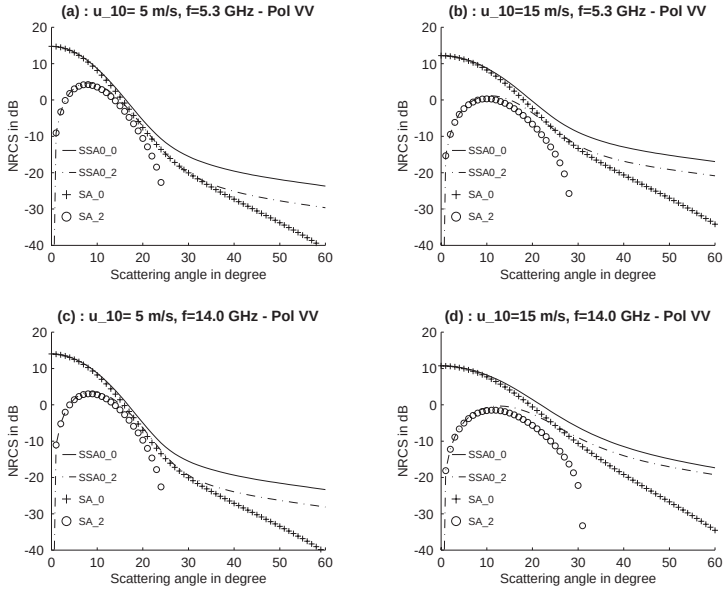

Figure 17. VV normal radar cross sections $\{\sigma^{,0}_{VV}, \sigma^{,2}_{VV}\}$ of {SSA0,SA} in C ($f = 5.3\,\mathrm{GHz}$, $\varepsilon_r = 67 + j35$, at the top) and Ku Bands ($f = 14\,\mathrm{GHz}$, $\varepsilon_r = 47 + j38$, at the bottom) versus the scattering angle for wind speeds $u_{10} = \{5, 15\}$ m/s with a dielectric anisotropic sea surface.

where $C_i(a, b, \phi)$ and $S_2(a, b, \phi)$ with $\{a = xr, b = K_\omega^2 f_{02}(r)\}$ are given in appendix B. Expanding C_i, and S_2, we can show that they expressed with respect to even harmonics $\cos(2n\phi)$. Consequently, as the SSA0 approach, the $\cos\phi$ term in (39) is equal to zero.

The identification of (46) with (39) yields

$$\begin{aligned}
\sigma^{SA,0} &= 2(K\cos\theta)^2 \exp(-K_\omega^2)|R_{H,V}|^2 \int_0^\infty \{\exp(K_\omega^2 f_{00}) \\
&\quad \cdot[J_0 I_0 + 4\sin\theta K \Re(R_{H,V} R_{H1,V1})/|R_{H,V}|^2 \\
&\quad \cdot I_1(R_{10} J_0 + R_{12} J_1)] - J_0\} r dr \qquad (46a) \\
\sigma^{SA,1} &= 0 \qquad (46b) \\
\sigma^{SA,2} &= 2(K\cos\theta)^2 \exp(-K_\omega^2)|R_{H,V}|^2 \int_0^\infty \{2J_2 I_1 + 4\sin\theta K \\
&\quad \cdot \Re(R_{H,V} R_{H1,V1})/|R_{H,V}|^2 \{[I_0 + I_2][R_{10} J_2 + R_{12}(J_3 - J_1)/2] \\
&\quad + 4R_{02} J_2 I_0/(xr^2)\}\} r \exp(K_\omega^2 f_{00}) dr \qquad (46c)
\end{aligned}$$

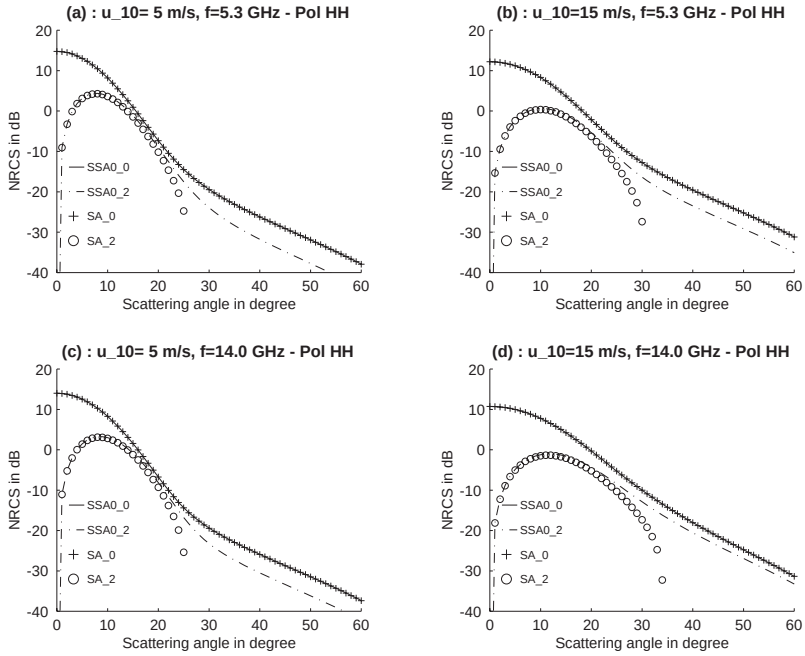

Figure 18. Same variation as Figure 17 for HH polarization.

where $\{J_i(\ldots), I_i(\ldots)\}$ depend on $\{xr, x_1 = K_\omega^2 f_{02}(r)\}$, respectively.

Figures 17–18 shows the predictions of the VV and HH normal radar cross sections $\{\sigma'^0, \sigma'^2\}$ of {SSA0,SA} in C ($f = 5.3\,\mathrm{GHz}$, $\varepsilon_r = 67 + j35$, at the top) and Ku Bands ($f = 14\,\mathrm{GHz}$, $\varepsilon_r = 47 + j38$, at the bottom) versus the scattering angle for wind speeds $u_{10} = \{5, 15\}\,\mathrm{m/s}$ with a dielectric anisotropic sea surface. As for an isotropic surface, for HH polarization the $\{\sigma_{HH}^{SSA0,2}, \sigma_{HH}^{SA,2}\}$ models coincide, whereas for the VV polarization the SA results are underestimated. When the scattering angle is close to the zero, $\sigma^{SSA0,2} \approx \sigma^{SA,2}$ and σ'^2 can be neglected, meaning that the backscattering coefficient does not depend on the wind direction.

In Figure 19, with the same parameters as Figures 17–18, for VV and HH polarizations, the SSA0 model is plotted versus the scattering angle with wind direction $\phi = \{0, 90\}^\circ$.

In Figure 20, the VV normal radar cross sections $\{\sigma_{VV}^{SSA0,0}, \sigma_{VV}^{SSA0,2}\}$ in C band are compared versus the scattering angle with experimental data. $\theta \in [18; 58]^\circ$, the wind speeds $u_{10} = \{5, 10, 15, 20\}\,\mathrm{m/s}$ and a dielectric anisotropic sea surface is considered. Experimental data are

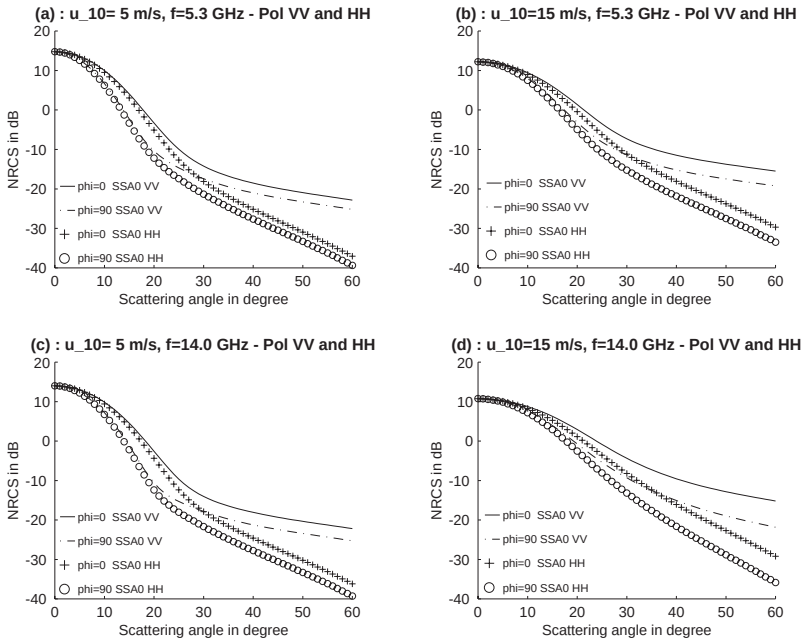

Figure 19. Comparison of the VV and HH normal radar cross section of the SSA0 model for wind direction $\phi = \{0, 90\}^\circ$. The parameters are the same as Figures 17 and 18.

calculated according to the CMOD2-I3 model (there is no model for the HH polarization for the C band). For small wind speeds, $\sigma_{VV}^{SSA0,2}$ overpredicts the measurements at low incidence angles and underpredicts it at high angles of incidence. For the isotropic part, $\sigma_{VV}'^{0}$ underestimates the experimental data.

In Figure 21, the comparison of the experimental data for $\phi = \{0, 180\}^\circ$ shows that the upwind and downwind asymmetry described by $\sigma_{pq}'^{1}$ is slightly.

In Figure 22, the backscattering coefficients $\{\sigma^{SSA0,0}, \sigma^{SSA0,2}\}$ for VV (one the left) and HH (on the right) polarizations in Ku band are compared with experimental data (SASS-II model [25]) versus the scattering angle. The wind speeds $u_{10} = \{5, 10, 15\}$ m/s. The deviation between the results and the measurements is greater for the HH polarization and decreases with the wind speed. As Figure 20, $\sigma^{SSA0,2}$ overpredicts the measurments. In a brief report, Voronovich et al [40] note comparable disparities between small-slope predictions and measured directionality at low incidence angles.

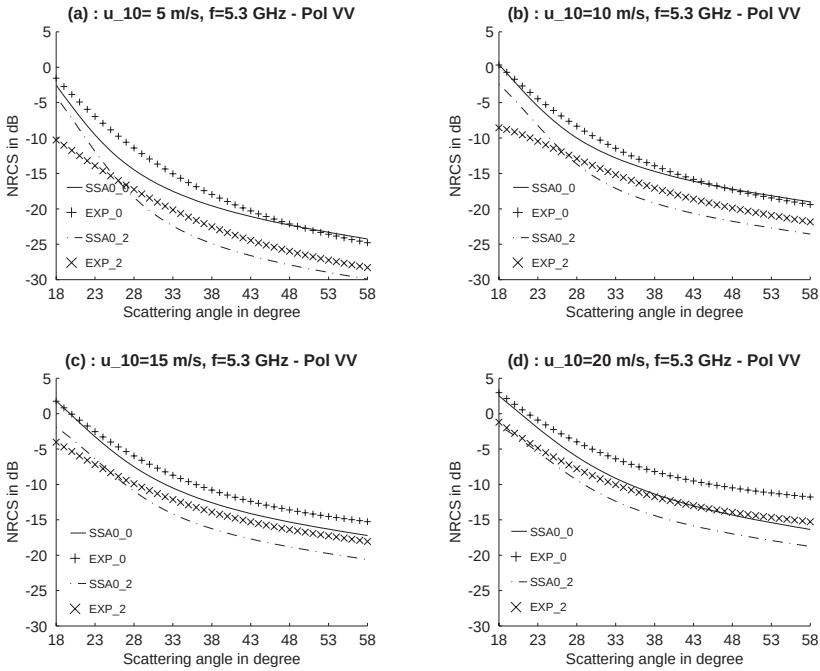

Figure 20. Comparison of the VV normal radar cross sections $\{\sigma_{VV}^{SSA0,0}, \sigma_{VV}^{SSA0,2}\}$ in C band with experimental data versus the scattering angle. The wind speeds $u_{10} = \{5, 10, 15, 20\}$ m/s and a dielectric anisotropic sea surface is considered. Experimental data are calculated according to the CMOD2-I3 model (there is no model for the HH polarization for the C band).

5. CONCLUSION AND DISCUSSION

We have calculated the backscattering cross section as a function of incidence angle in the upwind, downwind and cross-wind directions for Ku and C bands for three wind speeds of 5, 10 and 15 m/s and compared the results with averaged experimental data provided by the empirical models SASS-II [25] and CMOD2-I3 [24]. Calculations were performed with the help of the small-slope (SSA) [9–11] and the Kirchhoff (KA) approximations. Sea roughness was assumed to obey Gaussian statistics and the Elfouhaily et al [22] spectrum of roughness was used in numerical calculations. It is shown with the KA approach that the shadowing effect can be omitted for scattering angles of interest of remote sensing.

For an isotropic sea surface assumed to be perfectly conducting,

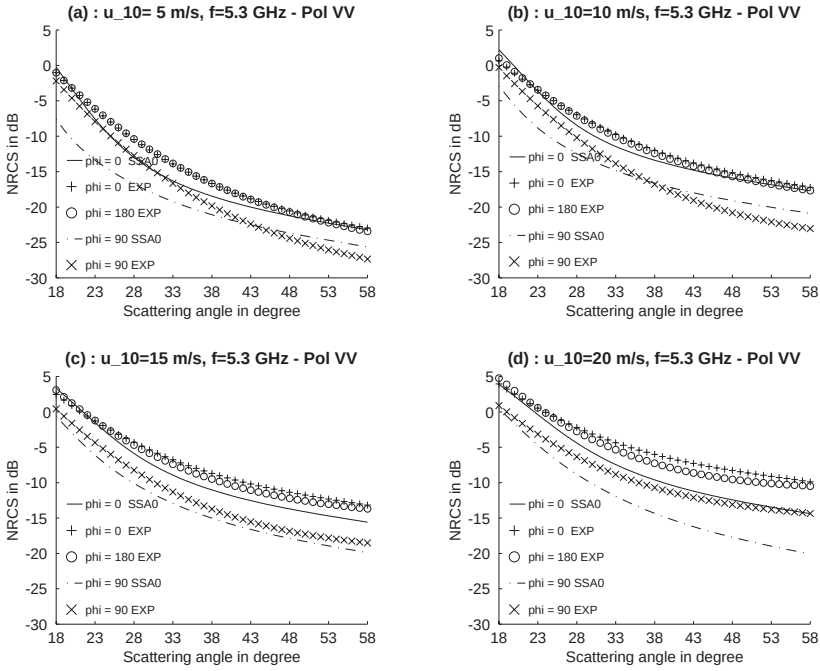

Figure 21. Comparison of the VV normal radar cross section σ_{VV}^{SSA0} in C band with experimental data (CMOD2-I3 model) versus the scattering angle for wind speeds $u_{10} = \{5, 10, 15, 20\}$ m/s and $\phi = \{0, 90, 180\}^\circ$. A dielectric anisotropic sea surface is considered, and σ_{VV}^{SSA0} with $\phi = 180^\circ$ is not plotted since it is equal to the one computed for $\phi = 0^\circ$.

the Kirchhoff approximation (KA) can be performed rigorously [18] without additional assumptions widely used in order to obtain the stationary phase (SP) method [19]. The simulations show that the first-order SSA approach denoted as SSA0 describes both the two regimes come from the gravity and capillary waves. At nadir-scattering angles, the SSA0 backscattering coefficient is close to the SP model which gives the contribution of the gravity waves, whereas for intermediate scattering angles, the Bragg regime is observed due to the capillary waves. With the KA formulation, a transition is observed with an underestimation of the radar cross section. Since the copolarization terms of SSA0 are equal to the ones of the small perturbation method, the backscattering coefficient for co-polarizations are not equal, whereas with the KA model, they are equal.

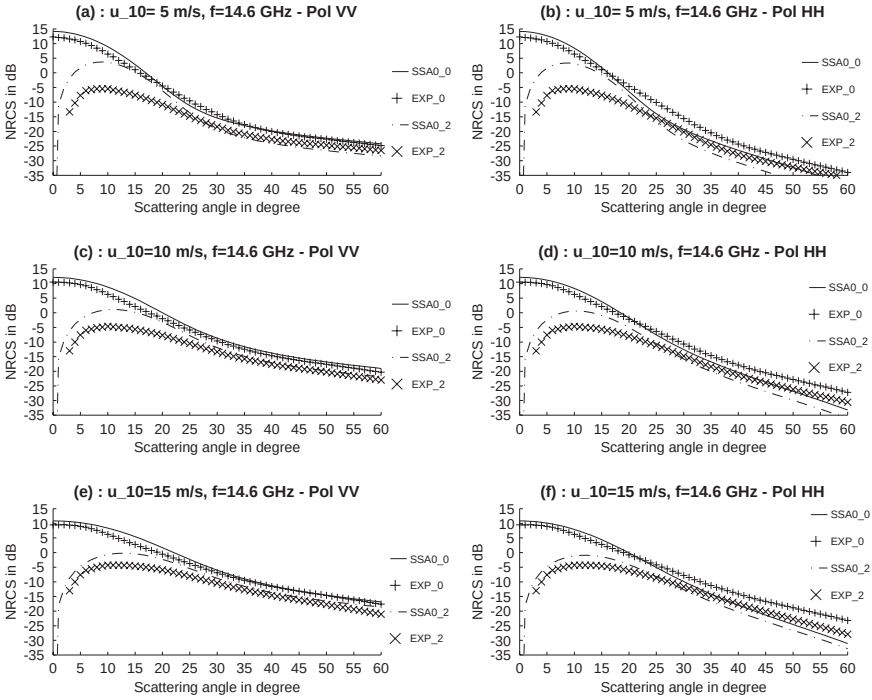

Figure 22. Comparison of the VV (on the left) and HH (on the right) normal radar cross sections $\{\sigma_{VV}^{SSA0,0}, \sigma_{VV}^{SSA0,2}\}$ in Ku band with experimental data (SASS-II model) versus the scattering angle. The wind speeds $u_{10} = \{5, 10, 15\}$ m/s and a dielectric anisotropic sea surface is considered.

For isotropic and anisotropic sea dielectric surfaces, the NRCS computed from the SA (KA of first-order according to the surface slopes) is similar to that SSA0 for HH polarization. The use of the polar coordinates allows to have an analytical expression of the harmonic magnitudes with respect to the wind direction. The backscattering coefficient requires then a single integration over the radial distance instead of four-fold integrations in cartesian coordinates with the SSA formulation. Since the sea spectrum is assumed to be symmetrical and real, with the SSA and SA approaches, the effect of the first azimuthal harmonic is nil.

The mean deviation given in Table 1 between the SSA0 results and measurements in C [24] and Ku [25] bands increases with the wind speed. As shown [14, 40] better agreement with measurements could

u_{10} in m/s	5	10	15	20
$\overline{\sigma_{VV}^{SSA0,0}}$ in dB	1.5	0.7	1.5	2.9
$\overline{\sigma_{VV}^{SSA0,2}}$ in dB	2.2	2.1	2.0	2.3

Table 1. Mean deviations $\overline{\sigma_{VV}^{SSA0,0}}, \overline{\sigma_{VV}^{SSA0,2}}$ between the SSA0 model and experimental data in C band for the VV polarization.

u_{10} in m/s	5	10	15
$\overline{\sigma_{VV}^{SSA0,0}}$ in dB	1.0	1.4	1.1
$\overline{\sigma_{VV}^{SSA0,2}}$ in dB	3.7	2.5	2.3
$\overline{\sigma_{HH}^{SSA0,0}}$ in dB	2.5	2.6	3.0
$\overline{\sigma_{HH}^{SSA0,2}}$ in dB	4.8	3.3	2.8

Table 2. Mean deviations $\overline{\sigma_{VV,HH}^{SSA0,0}}, \overline{\sigma_{VV,HH}^{SSA0,2}}$ between the SSA0 model and experimental data in Ku band for the VV and HH polarizations.

be obtained by modifying the sea spectrum. The modification means a more directional spectrum for long waves (at near-nadir scattering angles, the magnitude of the second azimuthal harmonic decreases), and a less directional spectrum for shorter waves (in the Bragg regime, the magnitude of the second azimuthal harmonic increases). This is consistent with Figure 6, where the surface slope standard deviations overestimate weakly the Cox and Munk models.

APPENDIX A. NORMAL RADAR CROSS SECTION OF SSA BY APPROXIMATING $\{|\Xi_{V,H}|^2\}$ BY THE FIRST TERM OF ITS TAYLOR SERIES

Approximating (34) $\{\Xi_{V,H}\}$ by the first term of its Taylor series expansion about the origin $\xi = 0$, we get

$$\Xi_V \approx 2\left[1 + \frac{k_0\xi\cos(\psi-\phi)}{2(k_0^2+K^2)}\right] \quad \Xi_H \approx 2\left[1 + \frac{k_0\xi\cos(\psi-\phi)}{2(k_0^2-K^2)}\right] \quad \text{(A1)}$$

This involves that

$$|\Xi_V|^2 \approx 4\left[1+\xi\cos(\psi-\phi)\Re\left(\frac{k_0}{k_0^2+K^2}\right)\right]$$
$$|\Xi_H|^2 \approx 4\left[1+\xi\cos(\psi-\phi)\Re\left(\frac{k_0}{k_0^2-K^2}\right)\right] \quad \text{(A2)}$$

Using the following relationship

$$\int_0^{2\pi}[1+\xi'\cos(\psi-\phi)]\exp[j\xi r\cos(\psi-\phi)]d\psi = 2\pi[J_0(\xi r)+j\xi' J_1(\xi r)\cos(\Phi-\phi)], \quad \text{(A3)}$$

Substituting (A2) into (35), and performing the integration over ψ, the exponential term $\exp\{\ldots\}$ of (35) is then expressed as

$$\exp\left\{\frac{K_\omega^2}{\omega^2}\int_0^\infty\left[M(\xi)J_0(\xi r)+\frac{j\cos(\Phi-\phi)}{K_{V,H}}\xi M(\xi)J_1(\xi r)\right]d\xi\right\} \quad \text{(A4)}$$

where

$$K_V=\Re[(k_0^2+K^2)/k_0] \quad K_H=\Re[(k_0^2-K^2)/k_0] \quad \text{(A5)}$$

The integration over ξ is expressed from $\{R_{00}(r), R_{10}(r)\}$ given by (25) and (27). Substituting then (A4) into (35), we get

$$\sigma^{SSA1} = \frac{(K\cos\theta)^2\exp(-K_\omega^2)|B_{H,V}|^2}{\pi} \cdot\int_0^\infty r dr\int_0^{2\pi}\exp[2jrK\sin(\theta)\cos(\Phi-\phi)](\exp\{K_\omega^2 \cdot[f_{00}(r)-j\sigma_x f_{10}(r)\cos(\Phi-\phi)/(\omega K_{V,H})]\}-1)d\Phi \quad \text{(A6)}$$

where

$$f_{00}(r)=R_{00}(r)/\omega^2 \quad f_{10}(r)=-R_{10}(r)/(\omega\sigma_x) \quad \text{(A7)}$$

The integration over Φ leads then to

$$\sigma^{SSA1} = 2(K\cos\theta)^2\exp(-K_\omega^2)|B_{H,V}|^2\int_0^\infty\{\exp(K_\omega^2 f_{00}) \cdot J_0(2rK\sin\theta-K_\omega^2 f_{10}\sigma_x/[\omega K_{V,H}]) -J_0(2rK\sin\theta)\}rdr \quad \text{(A8)}$$

APPENDIX B. ANGULAR INTEGRATIONS FOR A TWO-DIMENSIONAL SEA SURFACE

We need to solve the following integral over Φ

$$C_0(a,b,\phi) = \frac{1}{2\pi}\int_0^{2\pi} \exp[ja\cos(\Phi-\phi) - b\cos(2\Phi)]d\Phi \tag{B1}$$

The complex exponential can be expressed as [38]

$$\begin{cases} \exp[ja\cos(\Phi-\phi)] = \sum\limits_{m=-\infty}^{\infty} j^m J_m(a)\exp[jm(\Phi-\phi)] \\ \qquad\qquad\qquad\qquad = J_0(x) + 2\sum_{m=1}^{\infty} j^m J_m(a)\cos[m(\Phi-\phi)] \\ \exp[-b\cos(2\Phi)] = \sum\limits_{n=-\infty}^{\infty} j^n J_n(jb)\exp(2jn\Phi) \\ \qquad\qquad\qquad\qquad = J_0(jy) + 2\sum_{n=1}^{\infty} j^n J_n(jb)\cos(2n\Phi) \end{cases} \tag{B2}$$

where J_m is the Bessel function of the first kind and order m. Substituting (B2) into (B1) and performing the integration over Φ we show

$$C_0 = J_0(a)J_0(by) + 2\sum_{m=1}^{\infty}\sum_{n=1}^{\infty}\delta(m-2n)\cos(2n\phi)J_m(a)J_n(jb)j^{m+n} \tag{B3}$$

where δ is the Dirac function. Using the relation $J_n(jb) = j^n I_n(b)$ where I_n denotes the Bessel function of the second kind and order n, we obtain

$$C_0(a,b,\phi) = J_0(a)I_0(b) + 2\sum_{n=1}^{\infty}\cos(2n\phi)J_{2n}(a)I_n(b) \tag{B4}$$

The computation of the normal cross section requires the knowledge of the following integrals

$$C_1(a,b,\phi) = \int_0^{2\pi} j\cos(\Phi-\phi)\exp[ja\cos(\Phi-\phi) - b\cos(2\Phi)]d\Phi \tag{B5}$$

$$C_2(a,b,\phi) = \int_0^{2\pi} j\cos(2\Phi)\cos(\Phi-\phi)\exp[ja\cos(\Phi-\phi) - b\cos(2\Phi)]d\Phi \tag{B6}$$

$$S_1(a,b,\phi) = \int_0^{2\pi} \sin(2\Phi)\exp[ja\cos(\Phi-\phi) - b\cos(2\Phi)]d\Phi \tag{B7}$$

$$S_2(a,b,\phi) = \int_0^{2\pi} j\sin(\Phi-\phi)\sin(2\Phi)\exp[ja\cos(\Phi-\phi)-b\cos(2\Phi)]d\Phi \tag{B8}$$

Noting from (B1) that $C_1 = \partial C_0/\partial a$ and $C_2 = -\partial C_1/\partial b$, we show from (B4)

$$\begin{aligned} C_1(a,b,\phi) &= -J_1(a)I_0(b) + \sum_{n=1}^{\infty}\cos(2n\phi) \\ &\quad \cdot[J_{2n-1}(a) - J_{2n+1}(a)]I_n(b) \end{aligned} \tag{B9}$$

$$\begin{aligned} C_2(a,b,\phi) &= J_1(a)I_1(b) - \frac{1}{2}\sum_{n=1}^{\infty}\cos(2n\phi) \\ &\quad \cdot[J_{2n-1}(a) - J_{2n+1}(a)][I_{n-1}(b) + I_{n+1}(b)] \end{aligned} \tag{B10}$$

Using (B2), and the same way as C_0, we get

$$\begin{aligned} S_1(a,b,\phi) &= \frac{1}{2j}\sum_{n=-\infty}^{\infty} I_n(b)\exp(2jn\phi)[J_{2-2n}(a)\exp(-2j\phi) \\ &\quad -J_{-2-2n}(a)\exp(2j\phi)] \end{aligned} \tag{B11}$$

Noting from (B7)–(B8) that $aS_2 = \partial S_1/\partial\phi$, we show

$$\begin{aligned} S_2(a,b,\phi) &= \frac{1}{a}\sum_{n=-\infty}^{\infty} I_n(b)\exp(2jn\phi)[J_{2-2n}(a)(n-1)\exp(-2j\phi) \\ &\quad -J_{-2-2n}(a)(n+1)\exp(2j\phi)] \end{aligned} \tag{B12}$$

REFERENCES

1. Beckmann, P. and A. Spizzichino, *The Scattering of Electromagnetic Waves from Rough Surfaces, Part I: Theory*, Pergamon Press, London, 1963.
2. Ulaby, F. T., R. K. Moore, and A. K. Fung, *Microwave Remote Sensing, Vol. II*, Addison-Wesley, Reading, MA, 1982.
3. Olgilvy, J. A., *Theory of Wave Scattering from Random Rough Surfaces*, Adam Hilger, Bristol, Philadelphia, and New York, 1991.
4. Fung, A. K., C. Zuffada, and C. Y. Hsieh, "Incoherent bistatic scattering from the sea surface at L-band," *IEEE Trans. Geos. Rem. Sens.*, Vol. 39, No. 5, 1006–1012, 2001.

5. Rice, S. O., "Reflection of electromagnetic wave from slightly rough surfaces," *Symposium on the Theory of Electromagnetic Wave*, 351–378, 1950.
6. Thorsos, E. I. and S. L. Broschat, "The validity of the perturbation theory approximation for rough surface scattering using a Gaussian roughness spectrum," *J. Acoust. Soc. Am.*, Vol. 86, No. 1, 261–277, 1989.
7. Chevalier, B. and G. Berginc, "Small slope approximation method: scattering of a vector wave from 2D dielectric and metallic surfaces with Gaussian and non-Gaussian statistics," *SPIE Scattering and Surface Roughness*, Vol. III, 22–32, 2000.
8. Bahar, E. and B. S. Lee, "Radar scatter cross section for two-dimensional random surfaces—full wave solutions and comparisons with experiments," *Waves Random Media*, Vol. 6, 1–23, 1996.
9. Voronovich, A. G., "Wave scattering from rough surfaces," *Springer Series on Wave Phenomena*, Germany, 1994.
10. Voronovich, A. G., "Small slope approximation for electromagnetic wave scattering at a rough interface of two dielectric half-spaces," *Waves Random Media*, Vol. 4, 337–367, 1994.
11. Voronovich, A. G. and V. U. Zavorotny, "Theoretical model for scattering of radar signals in Ku- and C-bands from a rough sea surface with breaking waves," *Waves Random Media*, Vol. 11, 247–269, 2001.
12. Berginc, G., Y. Beniguel, and B. Chevalier, "Small slope approximation method: higher order contributions for scattering from 3-D surfaces," *SPIE Scattering and surface roughness*, Vol. II, 1999.
13. Berginc, G., Y. Beniguel, and B. Chevalier, "Extension of small-slope approximation method for 3-D scattering cross-section calculation of a rough convex object," *PIERS Proceedings*, Nantes, France, 582, 1998.
14. McDaniel, S. T., "Small-slope predictions of microwave backscatter from the sea surface," *Waves Random Media*, Vol. 11, 343–360, 2001.
15. Thorsos, E. I. and S. L. Broschat, "An investigation of the small slope approximation for scattering from rough surfaces, Part I: Theory," *J. Acoust. Soc. Am.*, Vol. 97, No. 4, 2082–2093, 1995.
16. Broschat, S .L. and E. I. Thorsos, "An investigation of the small slope approximation for scattering from rough surfaces, Part II: Numerical studies," *J. Acoust. Soc. Am.*, Vol. 101, No. 5, 2615–1625, 1997.

17. Semyonov, B., "Approximate computation of scattering electromagnetic waves by rough surface contour," *Radio Eng. Electron. Phys.*, Vol. 11, 1179–1187, 1966.
18. Bourlier, C., J. Saillard, and G. Berginc, "Theoretical study of the Kirchhoff integral from two-dimensional randomly rough surface with shadowing effect—application on the backscattering coefficient for a perfectly conducting surface," *Waves Random Media*, Vol. 11, 91–118, 2001.
19. Bourlier, C., J. Saillard, and G. Berginc, "Bistatic scattering coefficient from one- and two-dimensional random surfaces using the stationary phase and scalar approximation with shadowing effect—comparisons with experiments and application to the sea surface," *Waves Random Media*, Vol. 11, 119–147, 2001.
20. Bourlier, C., J. Saillard, and G. Berginc, "The shadowing function," *Progress in Electromagnetic Research*, J. A. Kong (ed.), Vol. 27, 226–287, EMW, Cambridge, 2000.
21. Bourlier, C., J. Saillard, and G. Berginc, "Study of the sea behavior," *Progress in Electromagnetic Research*, J. A. Kong (ed.), Vol. 27, 193–225, EMW, Cambridge, 2000.
22. Elfouhaily, T., B. Chapron, K. Katsaros, and D. Vandemark, "A unified directional spectrum for long and short wind-driven waves," *Journal. Geo. Res.*, Vol. 102, No. C7, 781–796, 1997.
23. Quilfen, Y., B. Chapron, T. Elfouhaily, K. Katsaros, and J. Tournadre, "Observation of tropical cyclones by high resolution scatterometry," *Journal. Geo. Res.*, Vol. 103, 7767–7786, 1998.
24. Bentamy, A., P. Queffeulou, Y. Quilfen, and K. Katsaros, "Ocean surface wind fields estimated from satellite active and passive microwave instruments," *IEEE Trans. Geosci. Remote Sens.*, Vol. 37, 2469–86, 1999.
25. Wentz, F. J., S. Peteherich, and L. A. Thomas, "A model function for ocean radar cross section at 14.6 GHz," *J. Geophys. Res.*, Vol. 89, 3689–3704, 1984.
26. Nghiem Fuk, S. V., K. Li, and G. Neumann, "The dependence of ocean backscatter at Ku-band on oceanic and atmospheric parameters," *IEEE Trans. Geosci. Remote Sens.*, Vol. 35, 581–600, 1997.
27. Cox, C. and W. Munk, "Statistics of the sea surface derived from sun glitter," *Journal Mar. Res.*, Vol. 13, 198–226, 1954.
28. Ellison, W., A. Balana, G. Delbos, K. Lamdaouchi, L. Eymard, C. Guillou, and C. Prigent, "New permittivity measurements of seawater," *Radio Sci.*, Vol. 33, 639–648, 1998.

29. Fung, A. K. and K. K. Lee, "A semi-empirical sea-spectrum model for scattering coefficient estimation," *IEEE Journal Oceanic Eng.*, Vol. 7, No. 4, 166–176, 1982.
30. Yoshimori, K., K. Itoh, and Y. Ichioka, "Optical characteristics of a wind-roughened water surface: a two dimensional theory," *Applied Optics*, Vol. 34, No. 27, 6236–6247, 1995.
31. Appel, J. R., "An improved model of the ocean surface wave vector spectrum and its effects on radar backscatter," *Journal Geo. Res.*, Vol. 99, No. C7, 1–21, 1994.
32. Lemaire, D., P. Sobieski, and A. Guissard, "Full-range sea surface spectrum in nonfully developed state for scattering calculations," *IEEE Trans. Geosci. Remote Sens.*, Vol. 37, 1038–1051, 1999.
33. Smith, B. G., "Lunar surface roughness, shadowing and thermal emission," *J. Geophysical Research*, Vol. 72, No. 16, 4059–4067, 1967.
34. Smith, B. G., "Geometrical shadowing of a random rough surface," *IEEE Trans. Ant. Prop.*, Vol. 15, 668–671, 1967.
35. Wagner, R. J., "Shadowing of randomly rough surfaces," *J. Acoust. Soc. Am*, Vol. 41, No. 1, 138–147, 1966.
36. Bourlier, C., J. Saillard, and G. Berginc, "Effect of correlation between shadowing and shadowed points on the Wagner and Smith monostatic one-dimensional shadowing function," *IEEE Trans. Ant. Prop.*, Vo. 48, 437–446, 2000.
37. Sancer, M. I., "Shadow-corrected electromagnetic scattering from a randomly rough surface," *IEEE Trans. Ant. Prop.*, Vol. 17, 577–585, 1969.
38. Abramovitz, M., I. A. Segun, *Handbook of Mathematical Functions*, Dover Publications, 1972.
39. Fung, A. K., *Microwave Scattering and Emission Models and Their Applications*, Artech House, Boston, MA, 1994.
40. Voronovich, V., U. Zavorotny, and V. G. Irisov, "Sea-roughness spectrum retrieval from radar and radiometric measurements," *Int. Geos. and Remote Sensing Symp.*, IEEE, Piscataway, NJ, 3102–3104, 2000.